

PROBING THE IGM-GALAXY CONNECTION AT $Z < 0.5$ I: A GALAXY SURVEY IN QSO FIELDS AND A GALAXY-ABSORBER CROSS-CORRELATION STUDY^{1,2}

HSIAO-WEN CHEN³ AND JOHN S. MULCHAEY⁴

Accepted for Publication in the Astrophysical Journal

ABSTRACT

We present an imaging and spectroscopic survey of galaxies in fields around QSOs HE 0226–4110, PKS 0405–123, and PG 1216+069. The fields are selected to have ultraviolet echelle spectra available, which uncover 195 Ly α absorbers and 13 OVI absorbers along the three sightlines. We obtain robust redshifts for 1104 galaxies of rest-frame absolute magnitude $M_R - 5 \log h \lesssim -16$ and at projected physical distances $\rho \lesssim 4 h^{-1}$ Mpc from the QSOs. HST/WFPC2 images of the fields around PKS 0405–123 and PG 1216+069 are available for studying the optical morphologies of absorbing galaxies. Combining the absorber and galaxy data, we perform a cross-correlation study to understand the physical origin of Ly α and OVI absorbers and to constrain the properties of extended gas around galaxies. The results of our study are (1) both strong Ly α absorbers of $\log N(\text{HI}) \geq 14$ and OVI absorbers exhibit a comparable clustering amplitude as emission-line dominated galaxies and a factor of ≈ 6 weaker amplitude than absorption-line dominated galaxies on co-moving projected distance scales of $r_p < 3 h^{-1}$ Mpc; (2) weak Ly α absorbers of $\log N(\text{HI}) < 13.5$ appear to cluster very weakly around galaxies; (3) none of the absorption-line dominated galaxies at $r_p \leq 250 h^{-1}$ kpc has a corresponding OVI absorber to a sensitive upper limit of $W(1031) \lesssim 0.03 \text{ \AA}$, while the covering fraction of OVI absorbing gas around emission-line dominated galaxies is found to be $\kappa \approx 64\%$; and (4) high-resolution images of five OVI absorbing galaxies show that these galaxies exhibit disk-like morphologies with mildly disturbed features on the edge. Together, the data indicate that OVI absorbers arise preferentially in gas-rich galaxies. In addition, tidal debris in groups/galaxy pairs may be principally responsible for the observed OVI absorbers, particularly those of $W(1031) > 70 \text{ m\AA}$.

Subject headings: cosmology: observations—intergalactic medium—quasars: absorption lines

1. INTRODUCTION

Traditional galaxy surveys trace large-scale structures visible through stellar light or radio emission of cold neutral gas. Stars and known gaseous components account for roughly 12% of all baryons in the local universe and the rest are thought to reside in ionized gaseous halos around galaxies or in intergalactic space (e.g. Fukugita 2004). In principle, the diffuse halo gas and intergalactic medium (IGM) can be probed by the forest of absorption line systems observed in the spectra of background QSOs. Studies of QSO absorption-line systems are therefore expected to provide important constraints for theoretical models that characterize the growth of large scale structures.

Indeed, the Ly α forest is found to account for $\gtrsim 95\%$ of the total baryons at redshift $z = 2 - 3$ (e.g. Rauch et al. 1997). In the nearby universe, Penton, Stocke, & Shull (2002, 2004) have argued that Ly α absorbers of neutral hydrogen column density $N(\text{HI}) \leq 10^{14.5} \text{ cm}^{-2}$ may contain between 20–30% of the total baryons based on a simple assumption for the cloud geometry. Various numerical sim-

ulations have further suggested that approximately 40% of the total baryons reside in diffuse intergalactic gas of temperature $T < 10^{5-6} \text{ K}$ (e.g. Davé et al. 2001; Cen & Ostriker 2006). This temperature range makes high-ionization transitions, such as OVI $\lambda\lambda 1031, 1037$ and Ne VIII $\lambda\lambda 770, 780$, ideal tracers of this warm-hot intergalactic medium (see e.g. Verner et al. 1994; Mulchaey et al. 1996; Tripp et al. 2000). However, recent studies have shown that roughly 50% of OVI absorbers are better explained by photo-ionized gas of cooler temperatures (e.g. Tripp et al. 2008; Thom & Chen 2008a,b). Therefore, the nature of these high-ionization systems does not appear to be unique.

Whether or not QSO absorption-line systems trace the typical galaxy population bears directly on the efforts to locate the missing baryons in the present-day universe (Persic & Salucci 1992; Fukugita, Hogan, & Peebles 1998), and to apply known statistical properties of the absorbers for constraining statistical properties of faint galaxies. This issue remains, however, unsettled (Lanzetta et al. 1995; Stocke et al. 1995; Chen et al. 1998, 2001a; Penton et al. 2002; Churchill et al. 2007). While nearly all galaxies within a projected physical distance of $\rho = 100 h^{-1}$ kpc from a background QSO have associated absorbers produced by CIV $\lambda\lambda 1548, 1550$ and Mg II $\lambda\lambda 2796, 2803$ (Chen et al. 2001b; Chen & Tinker 2008) and nearly all galaxies within $\rho = 180 h^{-1}$ kpc have associated Ly α absorbers of $N(\text{HI}) \geq 10^{14} \text{ cm}^{-2}$ (Chen et al. 1998, 2001a), not all Ly α absorbers have a galaxy found within $1 h^{-1}$ Mpc physical distance to a luminosity limit of $0.5 L_*$ (Morris et al. 1993; Tripp et al. 1998; Stocke et al. 2006). It is not clear whether these absorbers are associated with fainter galaxies or not related to galaxies at all. In addition, the origin of OVI absorbers in terms of their galac-

¹ Based in part on observations made with the NASA/ESA Hubble Space Telescope, obtained at the Space Telescope Science Institute, which is operated by the Association of Universities for Research in Astronomy, Inc., under NASA contract NAS 5-26555.

² Observations reported here were obtained in part at the Magellan telescopes, a collaboration between the Observatories of the Carnegie Institution of Washington, University of Arizona, Harvard University, University of Michigan, and Massachusetts Institute of Technology.

³ Dept. of Astronomy & Astrophysics and Kavli Institute for Cosmological Physics, University of Chicago, Chicago, IL, 60637, U.S.A. hchen@oddjob.uchicago.edu

⁴ The Observatories of the Carnegie Institution of Washington 813 Santa Barbara Street, Pasadena, CA 91101, U.S.A. mulchaey@ociw.edu

tic environment is also poorly quantified. While Stocke et al. (2006) found 95% of O VI absorbers at $z < 0.1$ are located at $\rho \lesssim 560 h^{-1} \text{ kpc}$ from an L_* galaxy, only three of the six O VI absorbers studied in Prochaska et al. (2006) have an L_* galaxy found at $\rho < 1 h^{-1} \text{ Mpc}$.

To understand the origin of QSO absorption-line systems, Chen et al. (2005) presented a pilot study of the galaxy–Ly α absorber cross-correlation function based on the Ly α absorbers and galaxies identified along a single sightline toward PKS0405–123. The two-point cross-correlation analysis provides a quantitative measure of the origin of the absorbers based on their clustering amplitude. More massive systems arise in relatively higher overdensity environments and are expected to exhibit stronger clustering amplitude than low-mass objects arising in lower-overdensity environments. A primary result of Chen et al. (2005) was that the cross-correlation function ξ_{ga} including only emission-line dominated galaxies and strong Ly α absorbers of $\log N(\text{HI}) \geq 14$ showed a comparable strength to the galaxy auto-correlation function ξ_{gg} on co-moving, projection distance scales $r_p \leq 1 h^{-1} \text{ Mpc}$, while there remained a lack of cross-correlation signal when using only absorption-line dominated galaxies. Absorption-line dominated galaxies have red colors and are presumably evolved early-type galaxies, while emission-line dominated galaxies are blue and presumably younger star-forming systems. Early-type galaxies are found to cluster more strongly than younger, star-forming galaxies (e.g. Madgwick et al. 2003; Zehavi et al. 2005), and are therefore expected to reside in regions of higher matter overdensity. The comparable correlation amplitudes of emission-line galaxies and strong Ly α absorbers therefore suggested that strong absorbers of $\log N(\text{HI}) \geq 14$ reside in the same overdensity regions as emission-line dominated galaxies. It appeared that these absorbers do not trace regions where more massive galaxies with dominant absorption spectral features reside.

This result of Chen et al. (2005) provided the first quantitative constraint on the origin of Ly α absorbers in terms of the significance of the underlying matter density fluctuations around the regions where they reside. It also offered a physical explanation for the on-average weaker clustering amplitude of Ly α absorbers relative to the clustering amplitude of the luminous galaxy population reported earlier (e.g. Morris et al. 1993). Wilman et al. (2007) performed a similar analysis based on a galaxy and Ly α absorber pair sample established over 16 QSO sightlines. While these authors concluded that a spectral-type dependent galaxy and Ly α cross-correlation function was not confirmed by their analysis, the two-dimensional cross-correlation function presented in Figure 4 of Wilman et al. clearly displays a strong signal between Ly α absorbers and emission-line galaxies that is absent in the cross-correlation function measured using only absorption-line galaxies.

To examine whether the initial results of Chen et al. (2005) obtained based on a single field are representative of the general Ly α absorber population, we have been conducting a deep, wide-area survey of galaxies in fields around QSOs at $z = 0.3 - 0.6$. The QSO fields are selected to have ultraviolet echelle spectra available from the Far Ultraviolet Spectroscopic Explorer (FUSE) and the Space Telescope Imaging Spectrograph (STIS) on board the Hubble Space Telescope (HST). The high-resolution UV spectra are necessary for finding intervening hydrogen Ly α and O VI absorbers to form a statistically representative sample (see e.g. Thom &

Chen 2008a; Tripp et al. 2008), as well as identifying their associated metal-line transitions for constraining the ionization state of the gas. The galaxy sample from our survey program therefore also allows us to expand upon the initial Ly α absorber study to understanding the galactic environment of ionized gas traced by the O VI absorbers. The primary objectives of our galaxy survey program are (i) to examine the physical origin of Ly α and O VI absorbers based on their respective clustering amplitudes, and (ii) to constrain the properties of extended gas around galaxies.

This paper is organized as follows. In Section 2, we describe the design of our galaxy survey program. In Section 3, we describe our observing program that includes both imaging observations, the selection of candidate galaxies, and multi-slit spectroscopic observations of three QSO fields. In Section 4, we summarize the results of the spectroscopic survey and examine the survey completeness. In Section 5, we summarize the properties of known absorption-line systems along individual QSO sightlines and present a new Ly α absorber catalog for the sightline toward PG 1216+069. Descriptions of individual fields are presented in Section 6. Results of a galaxy–absorber cross-correlation study are presented in Section 7, and their implications are discussed in Section 8. Finally, we summarize the main results of the paper in Section 9. We adopt a Λ CDM cosmology, $\Omega_M = 0.3$ and $\Omega_\Lambda = 0.7$, with a dimensionless Hubble constant $h = H_0/(100 \text{ km s}^{-1} \text{ Mpc}^{-1})$ throughout the paper.

2. GOALS AND DESIGN OF THE GALAXY SURVEY

The primary objectives of our galaxy survey program are (i) to examine the physical origin of Ly α and O VI absorbers based on their clustering amplitudes, and (ii) to constrain the properties of extended gas around galaxies. To reach the goals, we have been conducting a wide-area survey of galaxies in fields around QSOs at $z = 0.3 - 0.6$, for which echelle spectra at ultraviolet wavelengths are available from FUSE and HST/STIS. The high-resolution UV spectra are necessary for finding intervening hydrogen Ly α and O VI absorbers to form a statistically representative sample (see e.g. Thom & Chen 2008a; Tripp et al. 2008), as well as identifying their associated metal-line transitions for constraining the ionization state of the gas. The clustering amplitudes of Ly α and O VI absorbers are then determined based on their cross-correlation signals with the galaxies identified in the wide-field redshift survey.

To characterize the cross-correlation function of galaxies and Ly α /O VI absorbers, we aim to establish a statistically representative sample of L_* galaxies on scales of $\approx 1 - 4 h^{-1}$ co-moving Mpc from the QSO lines of sight over a redshift range of $z = 0.1 - 0.5$. These luminous galaxies are thought to reside at the peaks of the underlying dark matter density fluctuations with a small fraction ($\lesssim 20\%$) arising in group/cluster environments (Zheng et al. 2007). Therefore, they offer a unique tracer of the large-scale matter overdensity in the distant universe. Under the Λ CDM paradigm, the relative clustering amplitudes of QSO absorption-line systems with respect to these galaxies provide quantitative measures of the overdensities of the regions where the absorbers reside (Mo & White 2002; Tinker et al. 2005).

To examine the properties of extended gas around galaxies, we aim to establish a complete sample of sub- L_* galaxies at $z = 0.1 - 0.5$ within a projected co-moving distance of $r_p \approx 250 h^{-1} \text{ kpc}$ of the QSO lines of sight. The galaxy and absorber pair sample allows us to study the incidence and ex-

tent of ionized gas around galaxies of a range of luminosity and stellar content.

The short camera in the IMACS multi-object imaging spectrograph (Dressler et al. 2006) on the Magellan Baade telescope contains eight CCDs and has a plate scale of $0.2''$. It observes a sky area of $\approx 15'$ radius, corresponding to a co-moving distance of $3.6 h^{-1}$ Mpc at $z = 0.3$. In a single setup, IMACS provides the necessary field coverage to efficiently carry out our galaxy survey program. To reach the scientific objectives outlined above, we have selected three QSOs, HE 0226–4110 ($z_{\text{QSO}} = 0.495$), PKS 0405–123 ($z_{\text{QSO}} = 0.573$), and PG 1216+069 ($z_{\text{QSO}} = 0.331$), all of which are accessible from the Las Campanas Observatory. Together, these QSO sightlines provide the largest redshift pathlength available in the STIS echelle sample for the absorber survey (see Figure 3 of Thom & Chen 2008a), and allow us to examine possible field to field variation in the properties of absorbers and galaxies.

We have targeted the spectroscopic survey to reach (1) $> 80\%$ completeness for galaxies brighter than $R = 22$ and at an angular radius less than $\Delta\theta = 2'$ from the QSOs and (2) $\gtrsim 50\%$ completeness for galaxies brighter than $R = 20$ and at $\Delta\theta > 2'$. At $z = 0.2$, $R = 22$ corresponds to $\approx 0.04 L_*$ galaxies and $\Delta\theta = 2'$ corresponds to $\rho = 280 h^{-1}$ kpc. At $z = 0.5$, $R = 22$ corresponds to $\approx 0.3 L_*$ galaxies and $\Delta\theta = 2'$ corresponds to $\rho = 510 h^{-1}$ kpc. We note that the field around PKS 0405–123 has been studied by Chen et al. (2005) and Prochaska et al. (2006). The previous survey targeted galaxies brighter than $R = 20$, which was only sensitive to roughly L_* galaxies at $z = 0.5$. Our program has been designed to expand upon the earlier spectroscopic survey for measuring redshifts of fainter galaxies along the QSO line of sight.

3. OBSERVING PROGRAM

The observing program of the galaxy survey consists of three phases: (1) imaging observations of the QSO fields to identify candidate galaxies, (2) object selection for follow-up faint galaxy spectroscopy, and (3) multi-slit spectroscopic observations to measure the redshifts of the selected galaxies. In this section, we describe each of the three phases.

3.1. Imaging Observations and Data Reduction

Imaging observations of the fields around HE 0226–4110 and PG 1216+069 were necessary in order to identify galaxies for follow-up spectroscopy⁵. Faint galaxies in the field around PKS 0405–123 have been published in Prochaska et al. (2006), which are complete to $R = 22.5$. We have therefore selected our spectroscopic targets of this field from this galaxy catalog.

Optical images of the field around HE 0226–4110 were obtained on 2004 September 19, using the IMACS short camera and the *B*, *R*, and *I* filters on the Magellan Baade Telescope. Optical images of the field around PG 1216+069 were obtained on 2005 March 19, using the IMACS short camera and the *B*, *R*, and *I* filters. To increase the efficiency in the spectroscopic follow-up, the multi-bandpass *B*, *R*, and *I*

photometric measurements were necessary for selecting candidate galaxies at $z < 0.5$, excluding contaminating red stars and possible luminous high-redshift galaxies. The observations were carried out in a series of four to six exposures of between 300 and 500 s each, and were dithered by between 20 and 30 arcsec in space to cover the chip gaps between individual CCDs. All the imaging data were obtained under photometric conditions. We also observed standard star fields selected from Landolt (1992) through each of the *B*, *R*, and *I* filters on each night in order to calibrate the photometry in our targeted fields. Flat-field images were taken both at a flat screen at the secondary mirror of the Magellan Baade telescope and at a blank sky during evening twilight. A journal of the IMACS imaging observations is presented in Table 1, which lists in columns (1) through (6) the object field, instrument, filter, total exposure time, mean FWHM, and Date of observations, respectively.

The reduction and processing of IMACS imaging data were complicated because of the multi-CCD format and because of a substantial geometric distortion across the field of the IMACS short camera. Before stacking individual exposures, we first formed a single, geometrically-dewarped frame of every exposure according to the following steps. First, we subtracted the readout bias of individual CCDs using the overscan regions of the chips. Next, the bias subtracted frames were flattened using a super sky flat formed from median-filtering unregistered science exposures. We found that in the *B* and *R* images a super sky flat works more effectively than either dome flats or twilight flats in removing the gain variations between individual pixels. For images obtained through the *I* filter, however, the fringes in individual science exposures made it impossible to obtain an accurate flat-field image from the data. We therefore flattened the *I*-band exposures by first correcting the pixel-to-pixel variation using a median dome flat. The remaining fringes were then removed by subtracting a median *I*-band sky image formed from individual flattened science exposures.

Next we registered individual CCDs of each exposure using known stars found in the USNO A2.0 catalog. We formed a geometrically corrected mosaic frame of eight chips using the IRAF MSCRED package. The resulting mosaic frame contained calibrated astrometry with a typical r.m.s. scatter in stellar positions of $0.4''$. Finally, we combined individual mosaic frames to form a single stacked image of the QSO field for each of the *BRI* bandpasses. The final stacked images covered a contiguous sky area of $\approx 28 \times 28$ arcmin² and have mean point spread functions (PSFs) in the range of $\text{FWHM} = 0.7'' - 0.9''$ in the center of the IMACS field. Photometric calibrations were obtained using Landolt standard stars observed on the same night. The combined mosaic images reached 5σ limiting Vega magnitudes of $B = 24.5$, $R = 24.5$, and $I = 23.5$. False color images of the central $4' \times 4'$ regions around HE 0226–4110 and PG 1216+069 are presented in Figures 1 and 2, respectively.

Additional optical images of PKS 0405–123 and PG 1216+069 obtained with HST using the Wide Field and Planetary Camera2 (WFPC2) with the F702W filter were accessed from the Hubble Space Telescope (HST) data archive. Individual exposures of each field were reduced using standard pipeline techniques, registered to a common origin, filtered for cosmic-ray events, and stacked to form a final combined image. These high spatial resolution images allowed us to resolve faint galaxies close to the QSO line of sight and to study their morphology in detail (see Figures 8

⁵ We note that the field around PG 1216+069 is covered by the Sloan Digital Sky Survey (SDSS; York et al. 2000), which has a targeted imaging depth of $r' = 22.2$ (in the AB magnitude system). However, because of relatively large point spread functions (PSFs) with a mean full-width-half-maximum ($\text{FWHM} = 1.4''$), the available SDSS imaging data become significantly incomplete for detecting distant faint galaxies near the magnitude limit and for resolving objects near the QSO. Additional imaging data are therefore necessary for the purpose of our study.

TABLE 1
JOURNAL OF IMAGING OBSERVATIONS

Field (1)	Instrument (2)	Filter (3)	Exposure Time (s) (4)	FWHM (arcsec) (5)	Date (6)
HE 0226–4110 ($z_{\text{QSO}} = 0.495$)	IMACS	<i>B</i>	1200	0.8	2004-09-19
	IMACS	<i>R</i>	1200	0.7	2004-09-19
	IMACS	<i>I</i>	3000	0.7	2004-09-19
PKS 0405–123 ($z_{\text{QSO}} = 0.573$)	HST/WFPC2	F702W	2400	0.1	1996-01-08
	HST/WFPC2	F702W	2100	0.1	1998-09-16
	HST/WFPC2	F702W	2100	0.1	1998-09-23
PG 1216+069 ($z_{\text{QSO}} = 0.331$)	IMACS	<i>B</i>	1200	0.9	2005-03-19
	IMACS	<i>R</i>	1200	0.7	2005-03-19
	IMACS	<i>I</i>	3000	0.8	2005-03-19
	HST/WFPC2	F702W	2100	0.1	1998-03-30
	HST/WFPC2	F702W	2100	0.1	1999-04-18

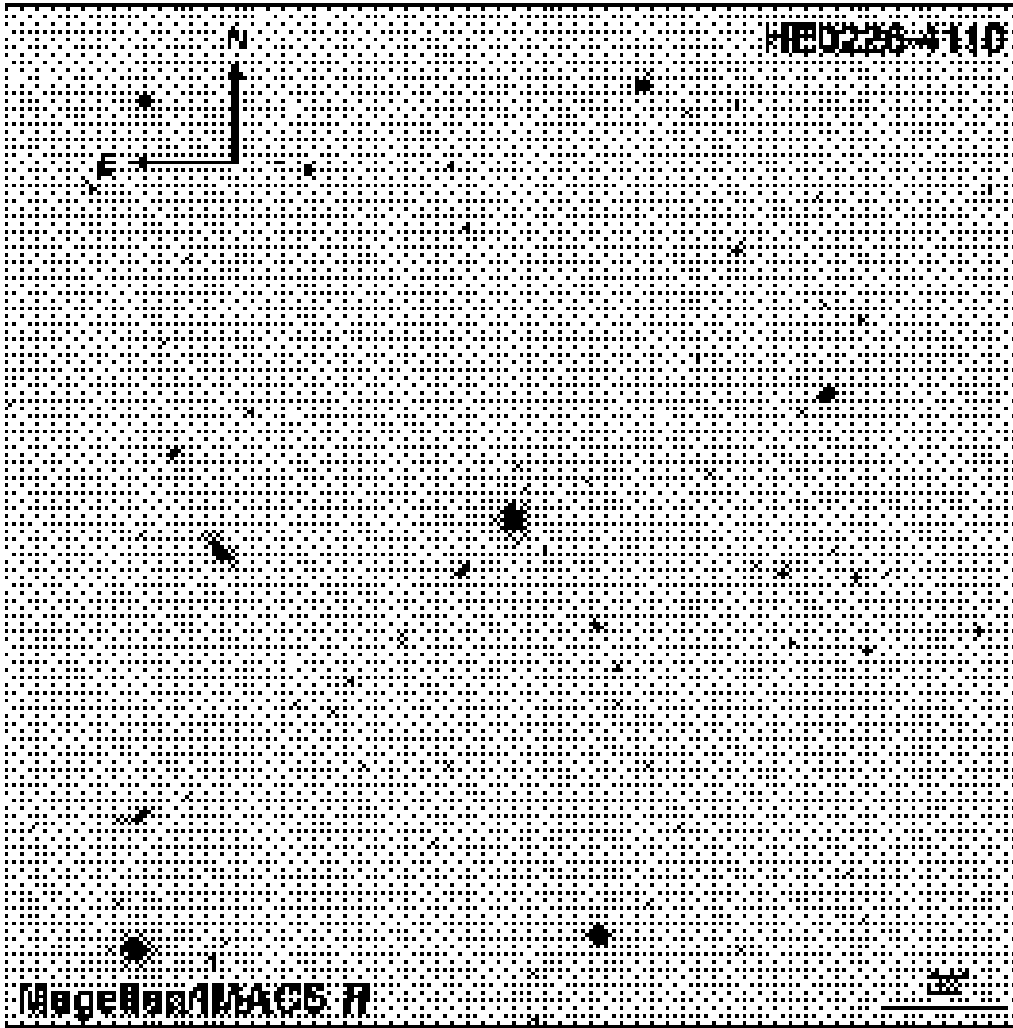


FIG. 1.— A combined IMACS *R*-band image of the center $4' \times 4'$ field around HE 0226–4110 ($z_{\text{QSO}} = 0.495$). The QSO is at the center of the panel.

& 9 below). A journal of the HST/WFPC2 observations is presented in Table 1 as well.

3.2. Selection of Candidate Galaxies for Spectroscopic Follow-up

To select galaxies in the fields around HE 0226–4110 and PG 1216+069 for spectroscopic follow-up, we first identified objects in the stacked *R*-band mosaic image using the SExtractor program (Bertin & Arnout 1996). Next, we measured object magnitudes in the *B*, *R*, and *I* images using the isopho-

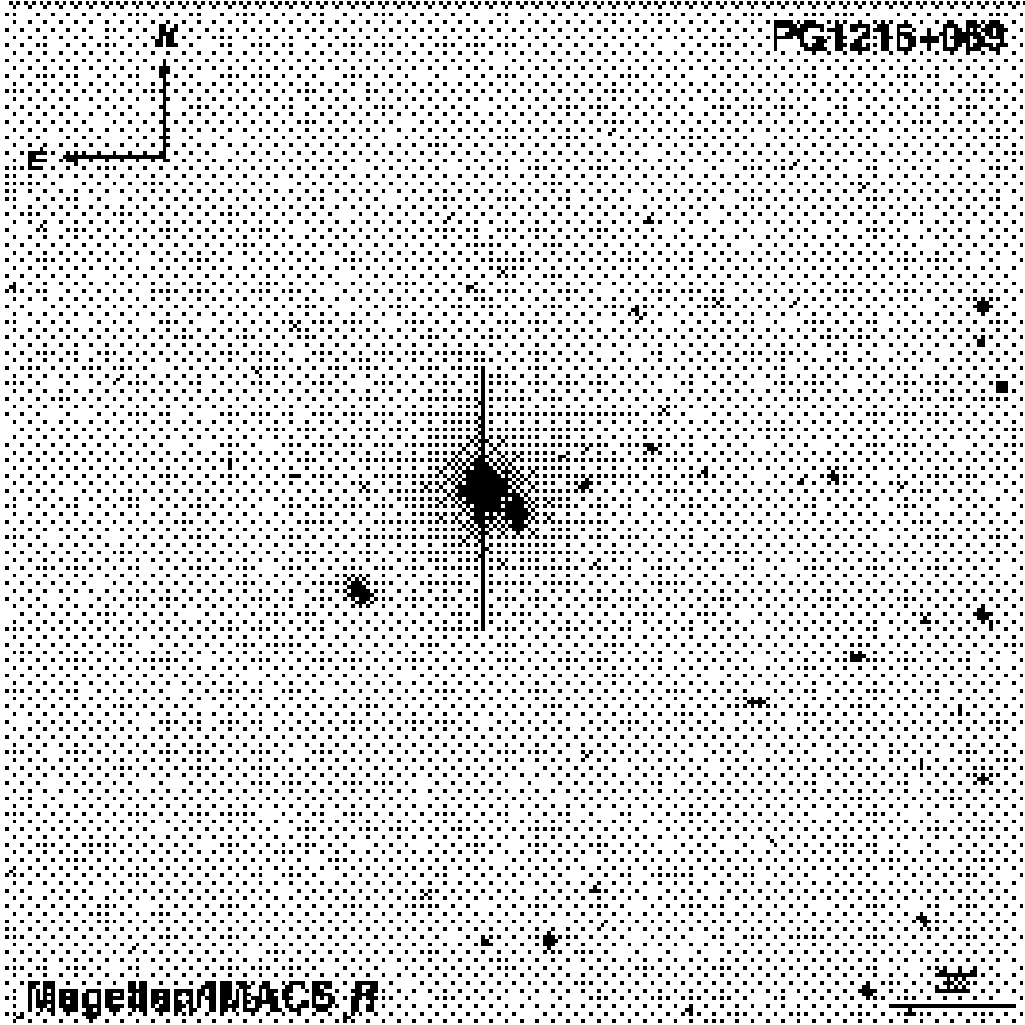


FIG. 2.— A combined IMACS *R*-band image of the center $4' \times 4'$ field around PG 1216+069 ($z_{\text{QSO}} = 0.331$). The QSO is at the center of the panel. The bright star at roughly $10''$ northeast of the QSO makes it challenging to accurately identify faint galaxies near the QSO sightline.

tal apertures of individual objects determined by SExtractor. This procedure yielded 948 and 1619 objects of $R = 16-22$ within $\Delta\theta = 11'$ angular radius from HE 0226-4110 and PG 1216+069, respectively. The difference in the object surface density underscores the significance of field to field variation. The sightline toward PG 1216+069 is known to pass through the outskirts of the Virgo cluster at $z = 0.004$ (and a projected physical distance $\rho \approx 1.4 h^{-1}$ Mpc). As discussed below, the results of our spectroscopic survey have also uncovered multiple large-scale overdensities along the sightline that contribute to the high surface density of galaxies in this field.

Separating stars and galaxies was challenging in these images, because of non-negligible PSF distortions toward the edge of the IMACS field. To optimize the efficiency of the spectroscopic observations, we applied the observed $B-R$ versus $R-I$ colors to exclude likely contaminations from faint red stars and high-redshift galaxies. Figure 3 shows the $B-R$ vs. $R-I$ color distribution of the objects found in the field around HE 0226-4110 (dots), together with stellar colors calculated using the stellar library compiled by Pickles (1998; star symbols) and simulated galaxy colors from

$z = 0$ (lower left) to $z = 1$ (upper right) in steps of $\Delta z = 0.1$ for E/S0 galaxies (filled circles), Sab (filled triangles), Scd (filled squares), and Irr (filled pentagon). The galaxy templates are adopted from Coleman et al. (1980). The straight line indicates our color selection, above which objects are likely to arise at $z \lesssim 0.7$ and represent candidate galaxies for follow-up spectroscopic observations with IMACS. This procedure yielded 776 and 1551 objects of $R = 16-22$ and $B-R+1.7 > 3.5(R-I)$ within $\Delta\theta = 11'$ angular radius from HE 0226-4110 and PG 1216+069, respectively.

The goals of our galaxy survey, as outlined in § 2, are (1) to establish a statistically representative sample of L_* galaxies for tracing the large-scale matter overdensities along the lines of sight toward the QSOs and (2) to identify a highly complete sample of sub- L_* galaxies within projected co-moving distance $r_p \approx 250 h^{-1}$ kpc from the QSO lines of sight for studying extended gas around individual galaxies and galaxy groups. In designing the multi-slit masks, we therefore aimed to include nearly all galaxies within $\Delta\theta = 2'$ of the background QSO. Because of spectral collisions between closely located objects, this goal dictates the number of masks required to reach a high survey completeness. We were able

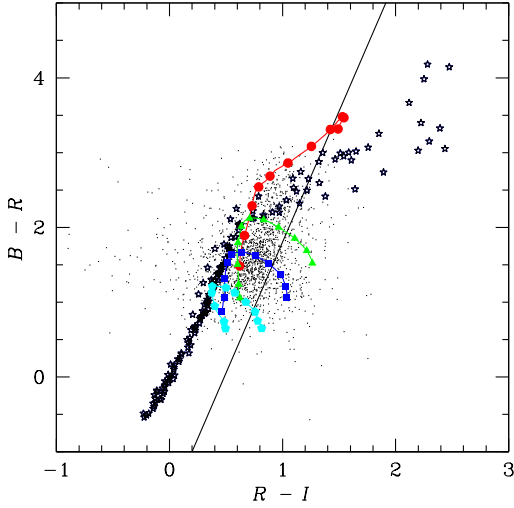


FIG. 3.— The $B-R$ vs. $R-I$ color distribution of the objects found in the field around HE 0226–4110 (dots). Optical colors of stars are shown in stellar symbols. These are calculated using the stellar library compiled by Pickles (1998). Simulated galaxy colors for different galaxy templates are also included for E/S0 (filled circles), Sab (filled triangles), Scd (filled squares), and Irr (filled pentagon) from $z = 0$ (lower left) to $z = 1$ (upper right) in steps of $\Delta z = 0.1$. The straight line indicates our color selection, above which objects are likely to arise at $z \lesssim 0.7$ and are included in the spectroscopic observations with IMACS.

to reach the goal in five IMACS masks and included 693 and 750 objects in the multi-slit spectroscopic observations of HE 0226–4110 and PG 1216+069, respectively⁶.

For the field around PKS 0405–123, we extracted 524 galaxies within $\Delta\theta = 11'$ of the QSO and brighter than $R = 22$ from the photometric catalog of Prochaska et al. (2006). These galaxies had not been observed in the previous survey. We aimed to complete the redshift survey of galaxies to $R \leq 22$ in this QSO field with IMACS observations. We designed five IMACS masks to observe 450 objects in this field.

3.3. Spectroscopic Observations and Data Reduction

Multi-slit spectroscopic observations of objects selected from the imaging program described in § 3.2 were carried out using IMACS and the short camera during three different runs in November 2004, May 2006, and April 2007. We were able to complete the observations of five masks for the field around HE 0226–4110, four masks in the field around PKS 0405–123, and five masks in the field around PG 1216+069. Each mask contained between 103 to 218 slitlets of $1.2''$ in width. Typical slit lengths were five arcseconds for compact sources. For extended objects, we adopted the Kron radius estimated in SExtractor and expanded by a factor of three to allow accurate sky subtraction. We used the 200 l/mm grism that offers a spectral coverage of $\lambda = 5000-9000 \text{ \AA}$ with $\approx 2 \text{ \AA}$ per pixel resolution. Observations of faint galaxies were carried out in a series of two to three exposures of between 1200 to 1800 s each. Observations of He-Ne-Ar lamps and a quartz lamp were performed every

hour for wavelength and flat-field calibrations. A journal of the IMACS spectroscopic observations is presented in Table 2, which lists in columns (1) through (7) the object field, instrument set-up, spectral resolution (FWHM), mask number, number of objects observed per mask, total exposure time, and Date of observations, respectively.

Additional spectroscopic observations of 27 objects at $\Delta\theta < 2'$ from HE 0226–4110 and eight objects from PKS 0405–123 were attempted in October 2007 and December 2008, using the Low Dispersion Survey Spectrograph 3 (LDSS3) on the Magellan Clay telescope. We included galaxies fainter than $R = 22$ and clearly visible near the QSO sight-lines in the LDSS3 observations, to further improve the survey depth in the immediate vicinity of the QSOs. LDSS3 observes a field of $8.3'$ diameter at a pixel scale of $0.189''$. We used the volume phase holographic (VPH) *blue* and VPH *all* grisms that cover a spectral range of $\lambda = 4000-6500 \text{ \AA}$ and $\lambda = 6000-9000 \text{ \AA}$, respectively, and $1.0'' \times 7''$ slitlets. The additional LDSS3 multi-slit spectroscopic observations allow us to reach 100% survey completeness of faint galaxies near the QSOs. A journal of the LDSS3 observations is included in Table 2 as well.

The multi-slit spectroscopic data were processed and reduced using the Carnegie Observatories System for MultiObject Spectroscopy (COSMOS) program⁷ that has been developed and tested by A. Oemler, K. Clardy, D. Kelson, and G. Walth. The program adopts the optical model of the spectrograph and makes initial guesses both for the slit locations in the 2D spectral frame and for the wavelength calibrations of individual spectra. These initial guesses are then further refined using known spectral lines in the He-Ne-Ar frame obtained close in time with the science data. The rms scatter of the wavelength solution is typically a fraction of a pixel, i.e. $\lesssim 1 \text{ \AA}$. Each raw frame of our spectral data was processed for bias subtraction and corrected for flat-fielding variations, following the standard procedure. Spectral extraction was performed using optimal weights determined according to the noise of relevant pixels. An error spectrum was generated from each raw frame, following noise counting statistics and the spectrum extraction procedure, and propagated through the pipeline. Finally, the extracted 1D spectra and their associated errors were flux-calibrated using a crude spectral sensitivity function calculated from the spectra of the alignment stars.

4. RESULTS OF THE SPECTROSCOPIC SURVEY

4.1. Redshift Measurements and Spectral Classification

The redshifts of objects were determined independently by each of us in two steps. First, we performed separate automatic χ^2 fitting routines that determine a best-fit redshift based on cross-correlating the flux-calibrated object spectrum with an input model template. One of the cross-correlation routines was written by D. Kelson. This routine adopts SDSS spectral templates⁸ for early-type (SDSS template # 24) and late-type galaxies (#28) as input models, and determines a best-fit redshift based on matching absorption or emission line features. The other cross-correlation software was written by one of us (HWC), which employs four galaxy eigen spectra kindly provided by S. Burles. These eigen templates were obtained from analyzing $> 100,000$ SDSS galaxy spectra, us-

⁶ Some objects were duplicated in different masks.

⁷ <http://www.lco.cl/lco/telescopes-information/magellan/magellan/instruments/imacs/cosmos/cosmos.html>

⁸ See <http://www.sdss.org/dr7/algorithms/spectemplates/index.html>

TABLE 2
JOURNAL OF MULTI-SLIT SPECTROSCOPIC OBSERVATIONS

Field (1)	Instrument/ Disperser (2)	FHWM Å (3)	Mask (4)	No. of Slitlets (5)	Exposure Time (s) (6)	Date (7)
HE 0226–4110 ($z_{\text{QSO}} = 0.495$)	IMACS/f2/2001	12	1	187	3600	2004 November
	IMACS/f2/2001	12	2	168	3600	2004 November
	IMACS/f2/2001	12	3	119	3600	2004 November
	IMACS/f2/2001	12	4	116	2400	2004 November
	IMACS/f2/2001	12	5	103	3600	2004 November
	LDSS3/VPH Blue	4.3	...	27	3600	2007 October
PKS 0405–123 ($z_{\text{QSO}} = 0.573$)	LDSS3/VPH All	12	...	27	3600	2008 December
	IMACS/f2/2001	12	1	159	3600	2004 November
	IMACS/f2/2001	12	2	141	4200	2004 November
	IMACS/f2/2001	12	3	134	2400	2004 November
	IMACS/f2/2001	12	5	48	2400	2004 November
	LDSS3/VPH All	12	...	8	3600	2008 December
PG 1216+069 ($z_{\text{QSO}} = 0.331$)	IMACS/f2/2001	12	1	218	3600	2006 May
	IMACS/f2/2001	12	2	199	7200	2007 April
	IMACS/f2/2001	12	3	182	3600	2006 May
	IMACS/f2/2001	12	4	142	5400	2007 April
	IMACS/f2/2001	12	5	151	3600	2006 May

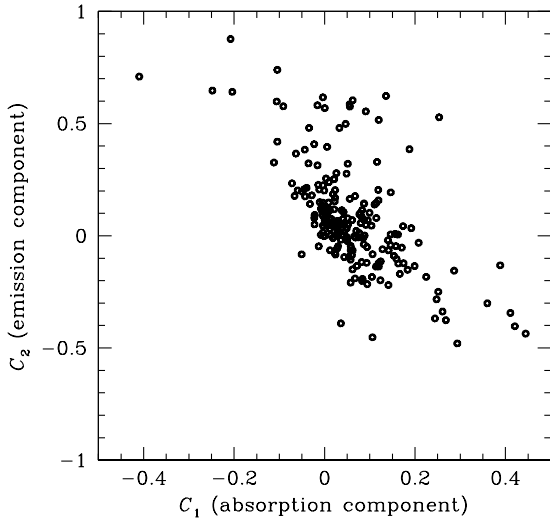


FIG. 4.— Relative significances between absorption (C_1) and emission (C_2) components for 220 galaxies in the field around PKS 0405–123. The absorption coefficient C_1 is determined by the best-fit coefficient of the first eigen spectrum. The emission coefficient C_2 is determined by the best-fit coefficient of the second eigen spectrum, corrected for the continuum slope by subtracting off the best-fit coefficients of the remaining two eigen spectra.

ing a principal component analysis (see e.g. Yip et al. 2004). The first two eigen spectra are characterized by predominantly absorption features and predominantly emission features, respectively. The last two eigen spectra offer additional modifications in the continuum slope. A linear combination of the four eigen function formed a model template to be compared with a flux-calibrated object spectrum, and a χ^2 routine was performed to determine the best-fit linear coefficients and redshift for each object.

Next, the best-fit redshifts returned from the cross-

correlation routines were then visually inspected by each of us to determine a final and robust redshift for every object. In some cases, the cross-correlation routines failed to identify a correct redshift due to contaminating residuals of bright skylines or imperfect background sky subtraction. We were able to recover the redshifts during this visual inspection process based on the presence of Ca II H&K, or the presence of H α and [N II]. A comparison between redshifts determined independently by the two of us shows a typical scatter of $|\Delta z| \approx 0.0003$, corresponding to $1\text{-}\sigma$ uncertainty of 70 km s^{-1} .

The procedure described above led to robust redshift measurements for 432 and 448 galaxies in the fields around HE 0226–4110 and PG 1216+069, respectively. In addition, we measured 224 new redshifts for galaxies in the field around PKS 0405–123, in comparison to 91 galaxy redshifts in the same area from Prochaska et al. (2006). The remaining galaxies turned out to have insufficient S/N in their spectra for a robust redshift measurement.

Spectral classification was guided by the relative magnitudes between the best-fit coefficients of the eigen spectra described above. These coefficients provide a quantitative evaluation of the fractional contributions from different spectral components in a galaxy, such as absorption spectra due to low-mass stars or emission spectra due to H II regions. The contribution due to absorption components may be determined by the best-fit coefficient of the first eigen spectrum (C_1). The contribution due to emission components may be determined by the best-fit coefficient of the second eigen spectrum, corrected for the continuum slope by subtracting off the best-fit coefficients of the remaining two eigen spectra (C_2). Figure 4 shows that despite a large scatter, there exists a linear distribution between emission C_2 and absorption C_1 components for 224 galaxies found in the field around PKS 0405–123. We classified galaxies with $C_1 > 0.09$ and $C_2 < 0.3$ as absorption-line dominated early-type galaxies and the rest as emission-line dominated late-type galaxies.

4.2. Survey Completeness and Galaxy Redshift Distribution

The results of our spectroscopic survey program in three QSO fields are summarized in Figure 5. For the field around HE 0226–4110, the open circles indicate the sky positions of all objects brighter than $R = 23$ and the closed circles indicate the ones with available spectroscopic redshifts. The QSO is at RA(J2000) = 37.0633 deg and Dec(J2000) = –40.9544 deg. For the fields around PKS 0405–123 and PG 1216+069, the open circles indicate the sky positions of all objects brighter than $R = 22$ and the closed circles indicate the ones with available spectroscopic redshifts. The QSOs are at RA(J2000) = 61.9518 deg and Dec(J2000) = –12.1935 deg, and RA(J2000) = 184.8372 deg and Dec(J2000) = 6.6440 deg, respectively.

We estimate the completeness of our survey by calculating the fraction of photometrically identified galaxies that have available spectroscopic redshifts. The calculations were performed for different minimum brightness in the R band and at different angular distances $\Delta\theta$ to the QSO. The results are presented in the top panels of Figure 6. We find that our survey is most complete in the field around HE 0226–4110, reaching 100% completeness for galaxies brighter than $R = 23$ at angular distances $\Delta\theta \leq 2'$. For PKS 0405–123 and PG 1216+069, we have also reached 100% completeness for galaxies brighter than $R = 20$ (solid lines), $> 80\%$ at $R = 21$ (dotted lines) and $> 60\%$ at $R = 22$ (dash-dotted lines) in the inner $2'$ radius. The survey completeness becomes $\approx 50\%$ at larger radii.

The bottom panels of Figure 6 show the redshift distributions of the spectroscopically identified galaxies in the three fields. The solid curve in each panel represents the model expectation from convolving a non-evolving rest-frame R -band galaxy luminosity function of Blanton et al. (2003), which is characterized by $M_{R_*} - 5 \log h = -20.4$, $\alpha = -1.1$, and $\phi_* = 0.015 h^3 \text{Mpc}^{-3}$, with the completeness functions displayed in the top panels. Redshift spikes indicate the presence of large-scale galaxy overdensities along the QSO lines of sight. The comparison between observations and model expectations in HE 0226–4110 and PG 1216+069 further demonstrates that the color selection criterion described in § 3.2 and Figure 3 has effectively excluded most galaxies at $z > 0.6$.

5. CATALOGS OF QSO ABSORPTION-LINE SYSTEMS

A necessary component of the galaxy–absorber cross-correlation analysis is an absorber catalog. A catalog of 57 Ly α absorbers along the sightline toward HE 0226–4110 has been published by Lehner et al. (2006). These Ly α absorbers exhibit a range of HI column density from $\log N(\text{HI}) = 12.5$ to $\log N(\text{HI}) = 15.1$ at $z_{\text{Ly}\alpha} = 0.017$ –0.4. We adopt their catalog in our cross-correlation analysis in this field. To summarize, the left panels of Figure 7 display the redshift distribution (top) and the cumulative $N(\text{HI})$ distribution function (bottom) of these absorbers.

The sightline toward PKS 0405–123 has been studied by Williger et al. (2006) and Lehner et al. (2007). We adopt the revised catalog of 76 Ly α absorbers from Lehner et al. (2007) in our analysis. These Ly α absorbers exhibit a range of HI column density from $\log N(\text{HI}) = 12.8$ to $\log N(\text{HI}) = 16.3$ at $z_{\text{Ly}\alpha} = 0.012$ –0.410. The middle panels of Figure 7 display their redshift distribution (top) and cumulative $N(\text{HI})$ distribution.

A systematic survey of Ly α absorbers for the sightline toward PG 1216+069 has only been conducted for strong systems by Jannuzi et al. (1998) in low-resolution (FWHM \approx

250 km s $^{-1}$) spectra obtained using the Faint Object Spectrograph. These authors identified nine strong Ly α absorbers with $\log N(\text{HI}) > 14$. To complete the study of low-column density gas ($\log N(\text{HI}) < 14$) along the sightline, we have conducted our own search of intervening Ly α lines in available echelle spectra of the QSO obtained by STIS.

Details regarding the reduction and processing of the STIS echelle spectra can be found in Thom & Chen (2008a). The final combined spectrum of PG 1216+069 covers a spectral range of $\lambda = 1160$ –1700 Å with a spectral resolution of ≈ 6.8 km s $^{-1}$ and has SNR of ≈ 7 per resolution element in most of the spectral region. To establish a complete catalog of Ly α absorbers, we first identify absorption features that are at $> 5\text{-}\sigma$ level of significance. Next, we identify known features due to either interstellar absorption of the Milky Way, or metal absorption lines and higher order Lyman series associated with known strong Ly α absorbers. We consider the remaining unidentified absorption lines as intervening Ly α absorbers. Finally, we perform a Voigt profile analysis using the VPFIT package⁹ for estimating the underlying $N(\text{HI})$ and the Doppler parameter b (e.g. Carswell et al. 1991). This procedure has yielded 66 Ly α absorbers of HI column density $\log N(\text{HI}) = 12.6$ –19.3 at $z_{\text{Ly}\alpha} = 0.003$ –0.321. The results of our search are presented in Table 3, which for each absorber lists the absorber redshift, $N(\text{HI})$ and the associated error, and b . The redshift distribution and cumulative $N(\text{HI})$ distribution of these Ly α absorbers are presented in the right panels of Figure 7.

For OVI absorbers along the sightlines toward the three QSOs in our survey, we adopt the catalog of Thom & Chen (2008a,b) and include absorbers at $z < 0.14$ from Tripp et al. (2008). There are five OVI absorbers known along the sightline toward HE 0226–4110, six OVI absorbers known along the sightline toward PKS 0405–123 (see also Prochaska et al. 2004), and two OVI absorbers known along the sightline toward PG 1216+069. The OVI absorber at $z = 0.1829$ along the sightline toward PKS 0405–123 shows two distinct components separated by ≈ 87 km s $^{-1}$ (see Thom & Chen 2008b; Prochaska et al. 2004). The OVI absorber at $z = 0.1236$ along the sightline toward PG 1216+069 also shows two dominant components well separated by ≈ 350 km s $^{-1}$ (see § 6.3 and Figure 12 below). We consider these components separate objects in the cross-correlation study presented in § 7. The redshifts of these OVI absorbers range from $z_{\text{OVI}} = 0.017$ to $z_{\text{OVI}} = 0.495$. The column densities of these absorbers range from $\log N(\text{OVI}) = 13.4$ to $\log N(\text{OVI}) = 14.7$. The redshift distribution of these OVI absorbers is shown in shaded histograms in the top panels of Figure 7.

6. DESCRIPTION OF INDIVIDUAL FIELDS

In this section, we review the galaxy and absorber properties in each individual field.

6.1. The Field toward HE0226–4110 at $z_{\text{QSO}} = 0.495$

The sightline toward HE 0226–4110 exhibits 57 Ly α absorbers (Lehner et al. 2006) and five OVI absorbers (Tripp et al. 2008; Thom & Chen 2008a,b) over the redshift range from $z_{\text{Ly}\alpha} = 0.017$ to $z_{\text{Ly}\alpha} = 0.4$. The column density of these Ly α absorbers span a range from $\log N(\text{HI}) = 12.5$ to $\log N(\text{HI}) = 15.1$, and the column density of the OVI absorbers span a range from $\log N(\text{OVI}) = 13.6$ to $\log N(\text{OVI}) =$

⁹ see <http://www.ast.cam.ac.uk/~rfc/vpfit.html>.

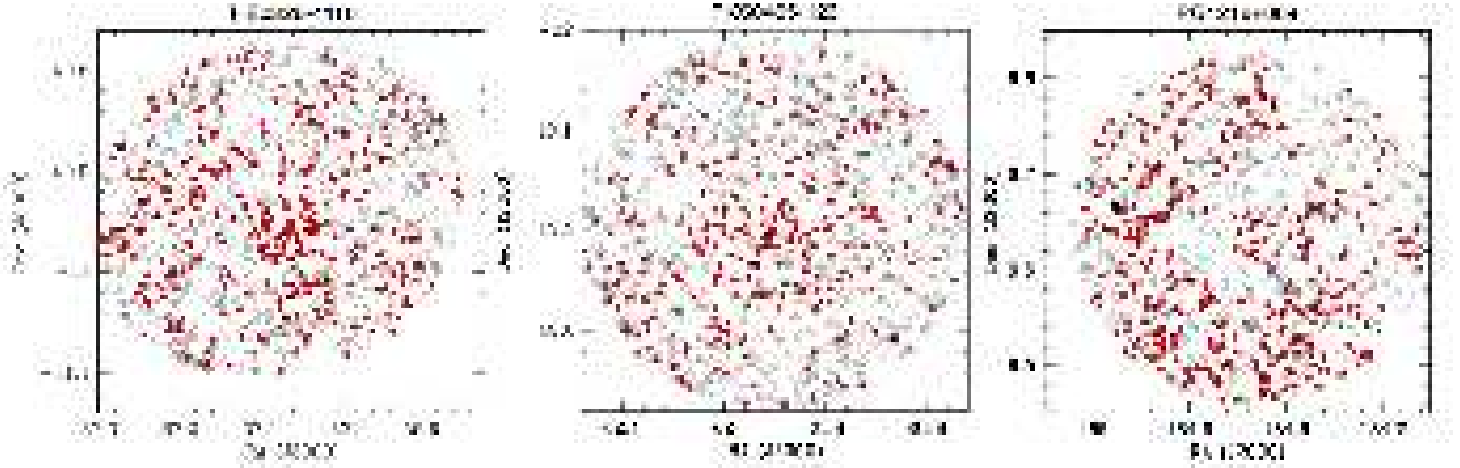


FIG. 5.— Summary of the spectroscopic survey in the fields around HE 0226–4110 (left), PKS 0405–123 (middle), and PG 1216+069 (right). Open circles represent all objects of $R \leq 23$ in HE 0226–4110, and $R \leq 22$ in PKS 0405–123 and PG 1216+069. Closed circles represent those with available spectroscopic redshifts. The QSOs are at RA(J2000) = 37.0633 deg and Dec(J2000) = –40.9544 deg, RA(J2000) = 61.9518 deg and Dec(J2000) = –12.1935 deg, and RA(J2000) = 184.8372 deg and Dec(J2000) = 6.6440 deg, respectively.

14.4. This field is particularly interesting because it exhibits a Ne VIII $\lambda\lambda 770,780$ absorber at $z = 0.20701$ (Savage et al. 2005), which is so far the only known detection of such high-ionization species in the IGM. The high ionization potential required to produce Ne⁷⁺ (207.28 e.V.) and the relatively large cosmic abundance of Ne make the Ne VIII doublet transitions a sensitive probe of warm-hot gas of $T = (0.5 - 1) \times 10^6$ K. Savage et al. (2005) performed a detailed analysis of the ionization state of the gas, taking into account the relative abundances of additional highly ionized species such as S VI and O VI, and concluded that the observations are best explained by a collisional ionized gas of $T = 5.4 \times 10^5$ K. While the detection of Ne VIII at $z = 0.207$ provides exciting support for the presence of warm-hot gas, this system remains unique and continuing efforts to search for more Ne VIII absorbers have uncovered no new systems (e.g. Lehner et al. 2006).

Our galaxy survey is most complete in the field around

HE 0226–4110, reaching 100% completeness for galaxies brighter than $R = 23$ at angular distances $\Delta\theta \leq 2'$ (upper-left panel of Figure 6). The redshift distribution shown in the bottom-left panel of Figure 6 displays clear galaxy overdensities at $z = 0.27$ and $z = 0.4$ in front of the QSO. While there are Ly α absorbers present at these redshifts, no OVI absorbers are found to coincide with these large-scale galaxy overdensities to the limit of $\log N(\text{OVI}) = 13.5$.

Figure 8 shows the redshifts of galaxies in the inner $2.7' \times 2.7'$ field around the QSO. We have been able to obtain high S/N spectra of galaxies at angular distance as close as $\Delta\theta \lesssim 3''$ to the background bright QSO. Galaxies with redshift coincide with known OVI absorbers ($|\Delta v| < 300 \text{ km s}^{-1}$) are marked by a rectangular box. A complete photometric and spectroscopic catalog of galaxies with $R \leq 23$ and at angular distance $\Delta\theta \leq 11'$ of the QSO is available electronically at http://lambda.uchicago.edu/public/cat/cat_0226.html. An ex-

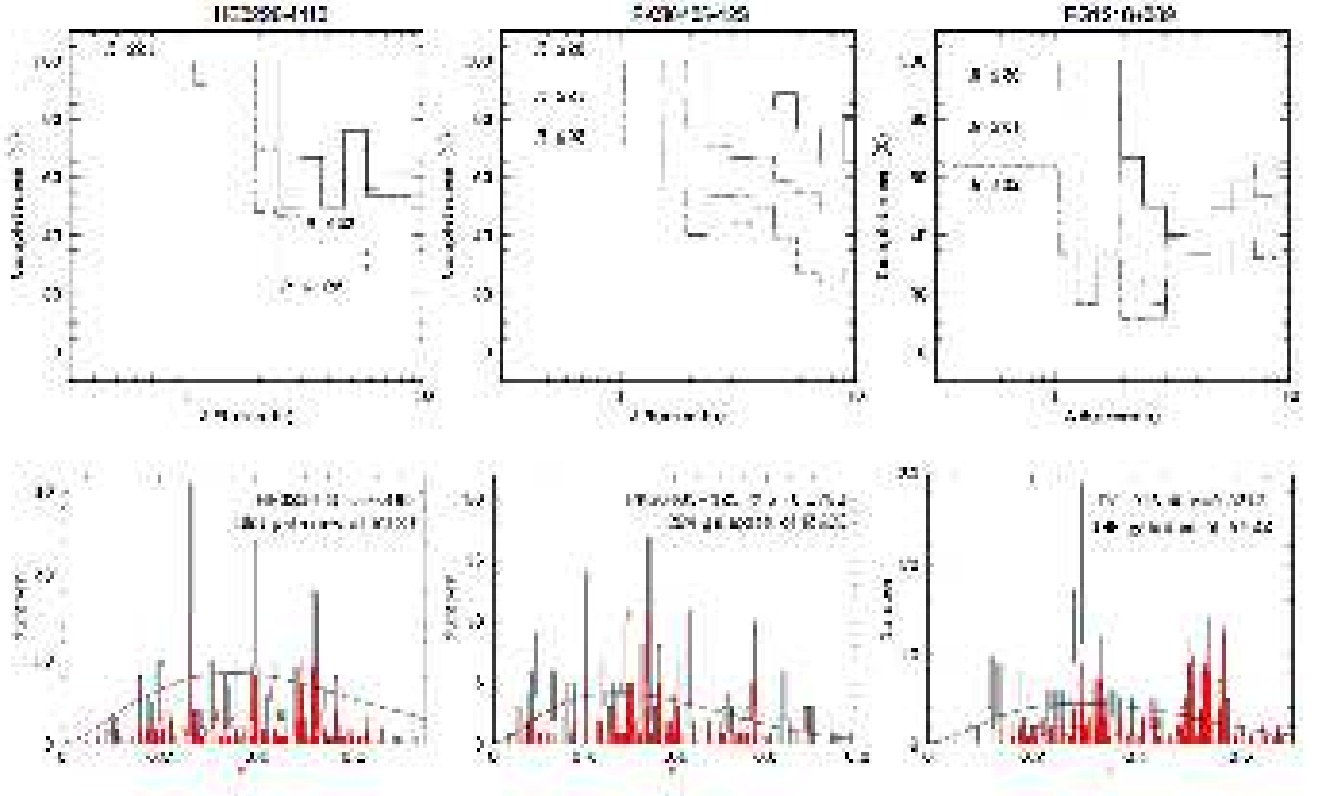


FIG. 6.— Summary of the survey completeness (top) and redshift distributions (bottom) of galaxies in the fields around HE0226–4110 (left), PKS0405–123 (middle), and PG1216+069 (right). The survey completeness was calculated for different brightness limits, from $R \leq 20$ (solid lines), to $R \leq 21$ (dotted lines) and to $R \leq 22$ (dash-dotted lines). The bottom panels show the redshift distributions of spectroscopically identified galaxies in the three fields, in comparison to model expectations (solid curves) based on a non-evolving rest-frame R -band galaxy luminosity function of Blanton et al. (2003) and the respective completeness functions displayed in the top panels. The redshift distribution of absorption-line dominated galaxies in each field is shown in solid histograms. Large-scale galaxy overdensities along the QSO lines of sight are evident through the presence of redshift spikes.

ample of the first 30 targets in the catalog is presented in Table 4, which lists from columns (1) through (13) the object ID, the right ascension (RA) and declination (Dec), the position offsets in RA ($\Delta\alpha$) and Dec ($\Delta\delta$) of the galaxy from the QSO, the angular distance to the QSO ($\Delta\theta$), the projected distance in physical h^{-1} kpc, the BRI magnitudes and uncertainties, the spectroscopic redshift z_{spec} (–1 indicates an absence of spectroscopic redshift measurement), spectral type, and rest-frame R -band absolute magnitude¹⁰.

Of the five OVI absorbers found along the sightline toward HE0226–4110, we have identified coincident galaxies at velocity offsets $|\Delta v| < 300 \text{ km s}^{-1}$ and projected physical distances $\rho \leq 250 h^{-1} \text{ kpc}$ for two absorbers, including the

Ne VIII absorber at $z = 0.207$. No galaxies are found near the OVI absorber at $z = 0.01746$ (Lehner et al. 2006; Tripp et al. 2008), although our spectroscopic survey only covers $\rho < 160 h^{-1} \text{ physical kpc}$ at this low redshift.

Three galaxies of $R = 20.3\text{--}21.9$ are found within $|\Delta v| < 300 \text{ km s}^{-1}$ and $\rho < 200 h^{-1} \text{ physical kpc}$ of the OVI and Ne VIII absorber at $z = 0.207$, all of which are sub- L_* galaxies with rest-frame R -band absolute magnitudes spanning a range from $M_R - 5 \log h = -17.2$ to $M_R - 5 \log h = -18.9$. The survey completeness rules out the presence of additional galaxies that are more luminous than $M_R - 5 \log h = -16.1$ within $\rho = 285 h^{-1} \text{ kpc}$. A detailed analysis of the galactic environment of the Ne VIII absorber is presented in Mulchaey & Chen (2009).

The nearest galaxy to the OVI absorber at $z = 0.32629$ (Thom & Chen 2008a,b) has $R = 23.0$ and $\rho = 381 h^{-1} \text{ physical kpc}$, with a corresponding rest-frame R -band absolute magnitude of $M_R - 5 \log h = -17.7$. The galaxy spectrum is dominated by absorption features. Three more galaxies are

¹⁰ The rest-frame R -band magnitude of each spectroscopically identified object was estimated based on the observed R -band magnitude and spectral type. For absorption-line dominated galaxies, we evaluate the k -correction using the early-type E/S0 and Sab galaxy templates from Coleman et al. (1980). For emission-line dominated galaxies, we evaluate the k -correction using the Irr templates.

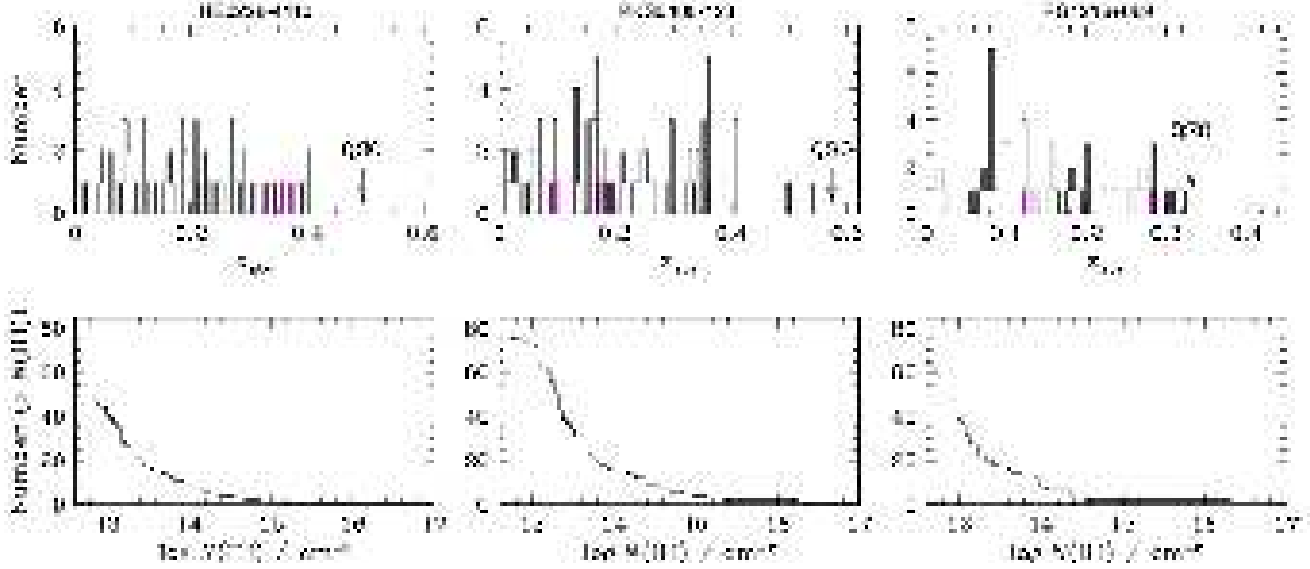


FIG. 7.— The redshift distribution (top) and cumulative $N(\text{HI})$ distribution (bottom) of $\text{Ly}\alpha$ absorbers identified along the sightline toward HE0226–4110 (left), PKS 0405–123 (middle), and PG 1216+069 (right). The shaded histograms in the top panels show the redshift distributions of OVI absorbers along the respective sightlines.

found at $|\Delta v| < 300 \text{ km s}^{-1}$ from the absorber redshift, but they are over $\rho = 840 h^{-1} \text{ kpc}$ to $\rho = 2.6 h^{-1} \text{ Mpc}$ physical distances away. The survey completeness rules out the presence of additional star-forming galaxies that are more luminous than $M_R - 5 \log h = -17.3$ within $\rho = 396 h^{-1} \text{ kpc}$.

The nearest galaxy to the OVI absorber at $z = 0.34034$ (Lehner et al. 2006; Tripp et al. 2008; Thom & Chen 2008a,b) has $R = 22.1$ and $\rho = 213 h^{-1}$ physical kpc, with a corresponding rest-frame R -band absolute magnitude of $M_R - 5 \log h = -18.3$. The galaxy spectrum is dominated by emission features. Two more galaxies are found at $|\Delta v| < 300 \text{ km s}^{-1}$ from the absorber redshift, and have $\rho = 432 h^{-1} \text{ kpc}$ and $\rho = 643 h^{-1} \text{ kpc}$ physical distances, respectively. The survey completeness rules out the presence of additional galaxies that are more luminous than $M_R - 5 \log h = -17.4$ within $\rho = 407 h^{-1} \text{ kpc}$.

The nearest galaxy to the OVI absorber at $z = 0.35529$ (Lehner et al. 2006; Tripp et al. 2008; Thom & Chen 2008a,b) has $R = 22.0$ and $\rho = 306 h^{-1}$ physical kpc, with a corresponding rest-frame R -band absolute magnitude of $M_R - 5 \log h = -18.5$. The galaxy spectrum is dominated by emission fea-

tures. Ten more galaxies are found at $|\Delta v| < 300 \text{ km s}^{-1}$ from the absorber redshift over a physical distance range of $\rho = 387 h^{-1} \text{ kpc}$ to $\rho = 1.8 h^{-1} \text{ Mpc}$. The survey completeness rules out the presence of additional galaxies that are more luminous than $M_R - 5 \log h = -17.5$ within $\rho = 419 h^{-1} \text{ kpc}$.

6.2. The Field toward PKS0405–123 at $z_{\text{QSO}} = 0.573$

The sightline toward PKS 0405–123 exhibits 76 $\text{Ly}\alpha$ absorbers (Lehner et al. 2006) and six OVI absorbers (Prochaska et al. 2004; Tripp et al. 2008; Thom & Chen 2008a,b) over the redshift range from $z_{\text{Ly}\alpha} = 0.012$ to $z_{\text{Ly}\alpha} = 0.538$. The column density of these $\text{Ly}\alpha$ absorbers span a range from $\log N(\text{HI}) = 12.5$ to $\log N(\text{HI}) = 16.3$, and the column density of the OVI absorbers span a range from $\log N(\text{OVI}) = 13.5$ to $\log N(\text{OVI}) = 14.7$.

The field around PKS0405–123 has been surveyed by Prochaska et al. (2006). This previous survey has yielded robust redshifts for 95% of all galaxies brighter than $R = 20$, corresponding to roughly L_* galaxies at $z = 0.5$. Our program expands upon the earlier spectroscopic survey for uncovering fainter galaxies along the QSO line of sight, reaching 100%

TABLE 3
IGM Ly α ABSORBERS IDENTIFIED ALONG THE SIGHTLINE TOWARD PG 1216+069

$z_{\text{Ly}\alpha}$ (1)	$\log N(\text{HI})$ (2)	$b \text{ (km s}^{-1}\text{)}$ (3)	$z_{\text{Ly}\alpha}$ (4)	$\log N(\text{HI})$ (5)	$b \text{ (km s}^{-1}\text{)}$ (6)
0.00362	13.32 ± 0.17	49 ± 24	0.13503 ^b	14.41 ± 0.04	35 ± 2
0.00630 ^{a,b}	19.32 ± 0.03	...	0.15475	13.07 ± 0.09	29 ± 7
0.01264	13.94 ± 0.03	40 ± 3	0.15512	12.75 ± 0.16	24 ± 11
0.01493	13.07 ± 0.10	34 ± 9	0.15576	12.77 ± 0.13	18 ± 7
0.01682	13.00 ± 0.14	59 ± 22	0.15601	13.10 ± 0.07	14 ± 3
0.01752	12.62 ± 0.18	20 ± 10	0.16076	13.14 ± 0.10	67 ± 19
0.02393	13.58 ± 0.03	26 ± 2	0.17993 ^b	13.97 ± 0.03	34 ± 2
0.05725	12.87 ± 0.12	35 ± 12	0.18026	13.23 ± 0.10	34 ± 9
0.06508	12.89 ± 0.11	25 ± 7	0.18071	13.48 ± 0.04	33 ± 3
0.07381	12.83 ± 0.12	23 ± 8	0.18698	13.26 ± 0.06	40 ± 6
0.07421	13.61 ± 0.03	35 ± 3	0.19007	12.96 ± 0.11	23 ± 7
0.07606	13.02 ± 0.08	31 ± 7	0.20040 ^b	13.98 ± 0.03	93 ± 7
0.08035	13.79 ± 0.24	45 ± 11	0.20114	13.17 ± 0.09	23 ± 5
0.08053 ^b	13.99 ± 0.15	32 ± 4	0.20442	12.94 ± 0.12	25 ± 8
0.08253	12.61 ± 0.19	16 ± 8	0.22189	13.34 ± 0.06	42 ± 7
0.08278	12.83 ± 0.16	35 ± 16	0.22578	12.99 ± 0.13	22 ± 9
0.08313	12.77 ± 0.12	16 ± 5	0.22728	13.09 ± 0.10	32 ± 9
0.08348	13.22 ± 0.07	37 ± 7	0.23035	12.67 ± 0.18	17 ± 9
0.08400	12.86 ± 0.18	64 ± 32	0.23641	13.45 ± 0.12	43 ± 15
0.08813	13.22 ± 0.07	54 ± 10	0.25035	12.93 ± 0.14	17 ± 6
0.09137	12.98 ± 0.08	30 ± 6	0.26267	13.12 ± 0.12	26 ± 9
0.09415	13.07 ± 0.10	40 ± 12	0.26624	12.93 ± 0.14	28 ± 10
0.09578	13.61 ± 0.03	39 ± 3	0.26763 ^b	14.01 ± 0.04	32 ± 2
0.09727	12.72 ± 0.20	44 ± 26	0.27154	12.81 ± 0.12	12 ± 4
0.09999	13.12 ± 0.05	20 ± 3	0.27352	14.43 ± 0.07	22 ± 3
0.10234	13.00 ± 0.15	78 ± 32	0.27865	12.98 ± 0.15	42 ± 17
0.10309	12.67 ± 0.15	15 ± 7	0.28108	12.72 ± 0.18	16 ± 8
0.10440	13.09 ± 0.08	32 ± 6	0.28226 ^b	16.34 ± 0.10	21 ± 2
0.12357	14.36 ± 0.08	29 ± 2	0.28298	12.88 ± 0.19	21 ± 10
0.12388 ^b	14.53 ± 0.14	28 ± 3	0.30394	13.40 ± 0.09	78 ± 20
0.12461 ^b	14.30 ± 0.02	53 ± 3	0.31377	12.97 ± 0.13	47 ± 17
0.12493	14.06 ± 0.07	20 ± 2	0.31857	13.23 ± 0.11	79 ± 24
0.12700	12.82 ± 0.09	20 ± 5	0.32102	12.83 ± 0.12	21 ± 7

^aThe measurement is adopted from Tripp et al. (2005).

^bThese lines have also been identified by Jannuzi et al. (1998) in low-resolution data obtained using the Faint Object Spectrograph.

completeness at $R = 20$ and $> 70\%$ at $R = 22$ within $\Delta\theta \leq 2'$ (upper-middle panel of Figure 6). The redshift distribution shown in the bottom-middle panel of Figure 6 displays numerous galaxy overdensities in front of the QSO, but only one OVI absorber is found to coincide with the large-scale galaxy overdensity at $z = 0.0966$.

Figure 9 displays a combined image of the field around PKS 0405–123, covering roughly a $2.7' \times 2.7'$ area. Galaxies with known spectroscopic redshifts are indicated by their redshifts to the left. Blue values represent redshift measurements obtained by previous authors (Spinrad et al. 1993; Prochaska et al. 2006). Red values represent new redshifts obtained in our survey. Galaxies with redshift coincident with known OVI absorbers ($|\Delta v| < 300 \text{ km s}^{-1}$) are marked by a rectangular box. While this field contains a relatively high surface density of galaxies, the majority of the galaxies turn out to reside in the QSO host environment. A complete photometric and spectroscopic catalog of galaxies with $R \leq 22$ and at angular distance $\Delta\theta \leq 11'$ of the QSO is available electronically at http://lambda.uchicago.edu/public/cat/cat_0405.html. An example of the first 30 targets in the catalog is presented in Table 5.

Of the six OVI absorbers found along the sightline toward PKS 0405–123, four are identified with coincident galaxies at $|\Delta v| < 300 \text{ km s}^{-1}$ and $\rho \leq 250 h^{-1} \text{ kpc}$. For the OVI ab-

sorber at $z = 0.0918$ (Prochaska et al. 2004), the closest galaxy found in previous surveys was at $\rho = 306 h^{-1} \text{ kpc}$ with $R = 19.7$ and $\Delta v = -341 \text{ km s}^{-1}$ (Prochaska et al. 2006). We have identified three new galaxies of $R = 21.3 - 21.9$ at $|\Delta v| = 27 - 275 \text{ km s}^{-1}$ and $\rho = 74 - 209 h^{-1} \text{ kpc}$ from the absorber, including one that is observed in the combined HST/WFPC2 image (left panel of Figure 10). All three galaxies are faint dwarfs with emission-line dominated spectral features (see the top three panels of Figure 15 below). The corresponding rest-frame R -band absolute magnitudes span a range from $M_R - 5 \log h = -15.4$ to $M_R - 5 \log h = -16.1$. The HST image presented in Figure 10 shows that the dwarf galaxy at $\rho = 73.5 h^{-1} \text{ kpc}$ exhibits a compact core with low-surface brightness emission extended to the north of the galaxy.

Only one galaxy is found within $|\Delta v| < 300 \text{ km s}^{-1}$ and $\rho < 200 h^{-1}$ physical kpc of the OVI absorber at $z = 0.09658$ (Prochaska et al. 2004). The galaxy has $R = 19.0$, corresponding to $M_R - 5 \log h = -18.2$ (Prochaska et al. 2006). Eight additional galaxies are found at $|\Delta v| < 300 \text{ km s}^{-1}$ from the absorber redshift and between $\rho = 257 h^{-1} \text{ kpc}$ to $\rho = 945 h^{-1} \text{ kpc}$ physical distances away.

The strong OVI absorber of $\log N(\text{OVI}) = 14.7$ at $z = 0.1671$ has been studied extensively by Chen & Prochaska (2000) and Prochaska et al. (2004). Two galaxies of $R = 17.43$

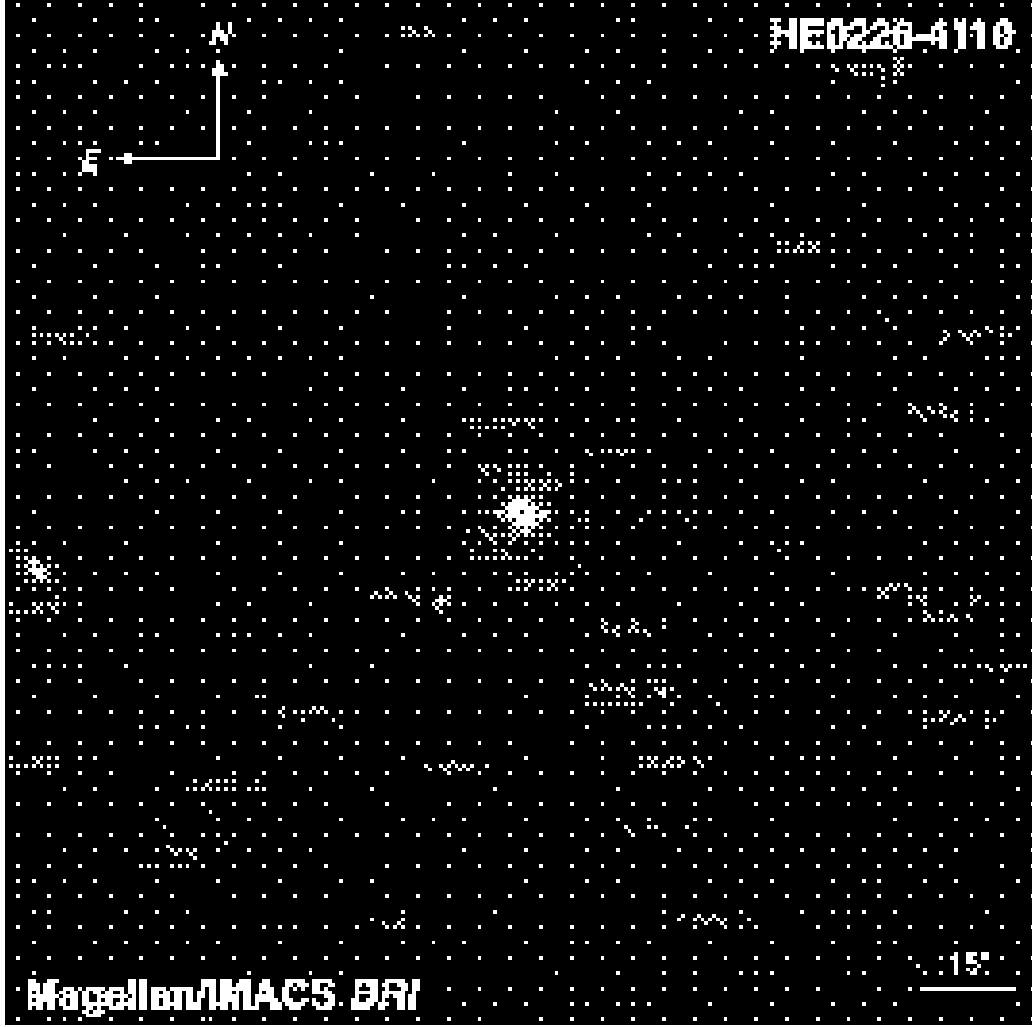


FIG. 8.— A summary of the spectroscopic survey of faint galaxies in the center $2.7' \times 2.7'$ field around HE 0226-4110 ($z_{\text{QSO}} = 0.495$). The false color image was produced using IMACS *B*, *R*, and *I* images from our preimaging data. We have reached 100% completeness for galaxies brighter than $R = 23$ in this area. Our best estimated redshifts are shown to the left of individual sources. Galaxies with redshift coincident with known OVI absorbers ($|\Delta v| < 300 \text{ km s}^{-1}$) are marked by a rectangular box. Most interestingly, at the location of the Ne VIII absorbers, $z = 0.20701$ (Savage et al. 2005), we found three galaxies at projected physical distances $\rho < 200 h^{-1} \text{ kpc}$.

and $R = 21.0$ are found within $|\Delta v| < 200 \text{ km s}^{-1}$ and $\rho < 100 h^{-1}$ physical kpc of the OVI absorber at $z = 0.1670$ (see the discussions in Chen & Prochaska 2000 and Prochaska et al. 2006). No additional galaxies are found within $\rho = 1 h^{-1}$ Mpc of the absorber. The luminous galaxy at $\Delta\delta = 40''$ (corresponding to $\rho = 80.9 h^{-1}$ kpc) from the QSO has $M_R - 5 \log h = -20.9$ and exhibits post starburst spectral features (Prochaska et al. 2006). The WFPC2 image presented in Figure 9 covers only part of the galaxy. A detailed examination of the WFPC2 image shows regular spiral structures with several compact H II regions along the spiral arms (center-left panel of Figure 10). The dwarf galaxy at $\rho = 67.8 h^{-1}$ kpc has $M_R - 5 \log h = -18.1$. The disk-like morphology appears to be mildly disturbed by a faint companion at the northeast edge (center-right panel of Figure 10).

No galaxies are found near the OVI absorber at $z = 0.1829$ (Prochaska et al. 2004; Tripp et al. 2008; Thom & Chen 2008a,b). The high completeness of our survey to $R = 22$ within $\Delta\theta = 2'$ suggests that the galaxies associated with the OVI ab-

sorber is likely fainter than $M_R - 5 \log h = -16.6$.

No galaxies are found near the OVI absorber at $z = 0.3633$ (Prochaska et al. 2004; Tripp et al. 2008; Thom & Chen 2008a,b). The high completeness of our survey to $R = 22$ within $\Delta\theta = 2'$ suggests that the galaxies associated with the OVI absorber is likely fainter than $M_R - 5 \log h = -18.5$.

The strong OVI absorber of $\log N(\text{OVI}) = 14.5$ at $z = 0.4951$ has been studied extensively by Howk et al. (2009). The early search by Prochaska et al. (2006) did not uncover any galaxies within $\rho = 2.6 h^{-1}$ Mpc. Our spectroscopic survey has uncovered a galaxy of $R = 22.63$ at $\Delta v = -181 \text{ km s}^{-1}$ and $\rho = 77 h^{-1}$ physical kpc from the absorber, with a corresponding rest-frame *R*-band absolute magnitude of $M_R - 5 \log h = -18.8$. The spectrum is dominated by emission-line features due to [O II], H γ , H β , and [O III] (see the 4th panel in Figure 15 below). The morphology appears to be extended in the HST image in Figure 10 (right panel). No additional galaxies are found at $|\Delta v| < 300 \text{ km s}^{-1}$ and $\rho < 1 h^{-1}$ Mpc.

TABLE 4
AN EXAMPLE OF THE PHOTOMETRIC AND SPECTROSCOPIC CATALOG OF OBJECTS IN THE FIELD AROUND HE0226-4110^a

ID (1)	RA(J2000) (2)	Dec(J2000) (3)	$\Delta\alpha$ ($''$) (4)	$\Delta\delta$ ($''$) (5)	$\Delta\theta$ ($''$) (6)	ρ (h^{-1} kpc) (7)	B (8)	R (9)	I (10)	z_{spec} (11)	Type ^b (12)	M_R $-5 \log h$ (13)
00443	02:29:21.173	-40:54:57.72	743.2	132.2	754.9	-1.00	22.740 ± 0.034	20.199 ± 0.006	18.865 ± 0.002	-1.0000	0	0.00
00542	02:29:19.348	-40:53:34.44	723.2	215.3	754.5	-1.00	23.831 ± 0.066	22.208 ± 0.024	21.471 ± 0.021	-1.0000	0	0.00
00551	02:29:19.107	-40:52:55.99	720.7	253.5	764.0	-1.00	23.595 ± 0.048	22.316 ± 0.022	21.853 ± 0.025	-1.0000	0	0.00
00562	02:29:19.090	-40:53:31.52	720.3	218.2	752.6	-1.00	25.019 ± 0.200	22.435 ± 0.031	21.368 ± 0.020	-1.0000	0	0.00
00578	02:29:19.162	-40:56:50.16	719.9	20.5	720.2	-1.00	22.480 ± 0.024	20.453 ± 0.006	19.700 ± 0.005	-1.0000	0	0.00
00595	02:29:19.137	-40:57:35.04	719.4	-24.1	719.8	-1.00	23.495 ± 0.066	21.802 ± 0.023	20.779 ± 0.015	-1.0000	0	0.00
00604	02:29:18.789	-40:57:29.05	715.5	-18.1	715.7	-1.00	24.723 ± 0.147	22.970 ± 0.048	22.043 ± 0.036	-1.0000	0	0.00
00676	02:29:18.104	-40:54:59.59	708.6	130.6	720.6	-1.00	22.600 ± 0.035	19.784 ± 0.004	18.270 ± 0.002	-1.0000	0	0.00
00685	02:29:17.937	-40:54:45.17	706.8	145.0	721.6	2422.79	22.052 ± 0.021	20.544 ± 0.009	19.855 ± 0.008	0.3347	2	-19.81
00686	02:29:18.299	-40:55:16.06	710.7	114.2	719.9	2838.03	23.014 ± 0.047	21.567 ± 0.021	21.286 ± 0.021	0.4329	2	-19.45
00693	02:29:17.587	-40:57:16.51	702.0	-5.6	702.0	-1.00	25.241 ± 0.267	22.480 ± 0.035	21.038 ± 0.016	-1.0000	0	0.00
00694	02:29:17.554	-40:58:39.99	701.1	-88.6	706.7	2640.43	23.287 ± 0.051	21.406 ± 0.014	20.639 ± 0.012	0.3957	1	-19.87
00699	02:29:17.643	-40:55:33.34	703.3	97.1	709.9	-1.00	24.376 ± 0.160	22.318 ± 0.038	22.169 ± 0.047	-1.0000	0	0.00
00731	02:29:17.061	-40:56:26.82	696.4	43.9	697.8	-1.00	24.646 ± 0.137	22.940 ± 0.045	22.294 ± 0.036	-1.0000	0	0.00
00733	02:29:17.169	-40:57:12.21	697.3	-1.2	697.3	-1.00	22.885 ± 0.041	19.942 ± 0.005	18.311 ± 0.002	-1.0000	0	0.00
00734	02:29:16.844	-40:55:31.43	694.3	99.1	701.3	-1.00	24.860 ± 0.220	22.249 ± 0.031	21.780 ± 0.028	-1.0000	0	0.00
00766	02:29:16.521	-40:52:29.86	691.7	279.7	746.1	1806.70	21.877 ± 0.016	19.504 ± 0.003	18.689 ± 0.002	0.2125	1	-20.00
00768	02:29:16.668	-40:55:35.82	692.2	94.7	698.7	-1.00	24.080 ± 0.137	21.605 ± 0.021	20.676 ± 0.012	-1.0000	0	0.00
00808	02:29:15.823	-40:58:33.06	681.7	-81.6	686.6	-1.00	24.985 ± 0.197	21.960 ± 0.020	20.525 ± 0.009	-1.0000	0	0.00
00811	02:29:15.782	-40:54:39.60	682.6	150.7	699.0	-1.00	23.763 ± 0.060	22.377 ± 0.029	21.780 ± 0.028	-1.0000	0	0.00
00820	02:29:15.782	-40:59:06.36	681.0	-114.7	690.6	2935.54	23.482 ± 0.060	21.809 ± 0.020	20.971 ± 0.016	0.4951	2	-19.58
00830	02:29:15.386	-40:52:03.47	679.0	306.1	744.8	-1.00	24.118 ± 0.095	22.542 ± 0.036	21.686 ± 0.026	-1.0000	0	0.00
00855	02:29:15.283	-40:59:43.43	675.2	-151.6	692.0	-1.00	24.084 ± 0.095	22.935 ± 0.049	21.812 ± 0.029	-1.0000	0	0.00
00861	02:29:14.925	-40:57:10.49	672.1	0.6	672.1	-1.00	24.847 ± 0.172	22.933 ± 0.046	21.701 ± 0.025	-1.0000	0	0.00
00862	02:29:14.974	-40:57:27.68	672.5	-16.5	672.7	-1.00	25.048 ± 0.182	22.919 ± 0.042	21.489 ± 0.018	-1.0000	0	0.00
00863	02:29:14.971	-40:52:05.68	674.3	303.9	739.7	-1.00	24.107 ± 0.099	22.633 ± 0.041	22.033 ± 0.036	-1.0000	0	0.00
00871	02:29:15.132	-40:57:02.04	674.4	9.0	674.5	-1.00	24.085 ± 0.081	22.600 ± 0.034	21.911 ± 0.029	-1.0000	0	0.00
00875	02:29:15.616	-40:59:51.01	678.9	-159.1	697.3	-1.00	22.372 ± 0.037	20.852 ± 0.015	20.062 ± 0.012	-1.0000	0	0.00
00879	02:29:15.087	-40:55:48.33	674.4	82.4	679.4	-1.00	23.696 ± 0.076	22.361 ± 0.035	21.305 ± 0.022	-1.0000	0	0.00
00885	02:29:14.503	-40:52:28.29	668.9	281.4	725.7	-1.00	25.539 ± 0.282	22.831 ± 0.038	21.314 ± 0.014	-1.0000	0	0.00

^a A complete catalog is available electronically at http://lambda.uchicago.edu/public/cat/cat_0226.html.

^b Spectral type of the galaxy: 1 → absorption-line dominated and 2 → emission-line dominated.

6.3. The Field toward PG1216+069 at $z_{\text{QSO}} = 0.3313$

The search of Ly α absorbers described in § 5 has identified 66 Ly α absorbers along the sightline toward PG 1216+069 over the redshift range from $z_{\text{Ly}\alpha} = 0.0036$ to $z_{\text{Ly}\alpha} = 0.321$ (Table 3). The column density of these Ly α absorbers span a range from $\log N(\text{HI}) = 12.6$ to $\log N(\text{HI}) = 19.3$. Two OVI absorbers are found at $z = 0.1242$ and $z = 0.2823$ with $\log N(\text{OVI}) = 14.7$ and $\log N(\text{OVI}) = 13.4$, respectively (Tripp et al. 2008; Thom & Chen 2008a,b)¹¹.

Our galaxy survey in the field around PG 1216+069 in the least incomplete of all three, reaching > 80% completeness for galaxies brighter than $R = 21$ at angular distances $\Delta\theta \leq 2'$ (upper-right panel of Figure 6). The redshift distribution shown in the bottom-right panel of Figure 6 displays a significant galaxy overdensity at $z = 0.26-0.28$ in front of the QSO. One of the two OVI absorbers does coincide with this large-scale galaxy overdensity. Figure 11 shows the redshifts of galaxies in the inner $2.7' \times 2.7'$ field around the QSO. We have not been able to obtain high quality spectra of galaxies at angular distance $\Delta\theta \lesssim 5''$ due to the presence of a bright star and the background QSO. Only one foreground galaxy is found at $\rho < 200 h^{-1}$ kpc. A complete photometric and

spectroscopic catalog of galaxies with $R \leq 22$ and at angular distance $\Delta\theta \leq 11'$ of the QSO is available electronically at http://lambda.uchicago.edu/public/cat/cat_1216.html. An example of the first 30 targets in the catalog is presented in Table 6.

A galaxy is identified at $|\Delta v| < 300 \text{ km s}^{-1}$ and $\rho \leq 250 h^{-1}$ kpc from the absorber at $z = 0.1242$ (see Chen et al. 2001a). The galaxy has $R = 19.3$, corresponding to $M_R - 5 \log h = -20.0$, and $\rho = 64 h^{-1}$ kpc. The morphology of the galaxy is indicative of a galaxy (at the southern edge) being tidally torn by a more massive galaxy during the process of merging (top-left panel of Figure 12). The spectrum of the system shown in the bottom left panel of Figure 12 exhibits prominent emission features, such as H α , [N II], and [S II], suggesting that the ISM is chemically enriched to solar metallicity. The large H α to H β line ratio also suggests the presence of substantial dust in the ISM.

The absorber at $z = 0.1242$ exhibits a complex absorption profile. We show in the right panel of Figure 12 the absorption features identified in the QSO spectra obtained using both HST/STIS and FUSE. Reduction and processing of the STIS spectra are described in Thom & Chen (2008). Reduction and processing of the FUSE spectra are described in Scott et al. (2004). The combined STIS spectrum has a spectral resolution of $\delta v \approx 6.8 \text{ km s}^{-1}$; the combined FUSE spectrum has a spectral resolution of $\delta v \approx 30 \text{ km s}^{-1}$.

At least four absorption components ($\Delta v = -158, -82, +120$ and $+188 \text{ km s}^{-1}$) are seen in the H I, C III, and O VI absorp-

¹¹ We note that Tripp et al. (2008) reported one more OVI absorber at $z = 0.26768$ along this sightline. However, the expected OVI 1037 transition falls at a wavelength that has been contaminated by a saturated Ly β feature at $z = 0.2819$. No other metal absorption lines are found for the absorber to confirm the nature of the presumed OVI 1031 feature. We therefore consider this absorption feature as Ly α at $z = 0.0760$.

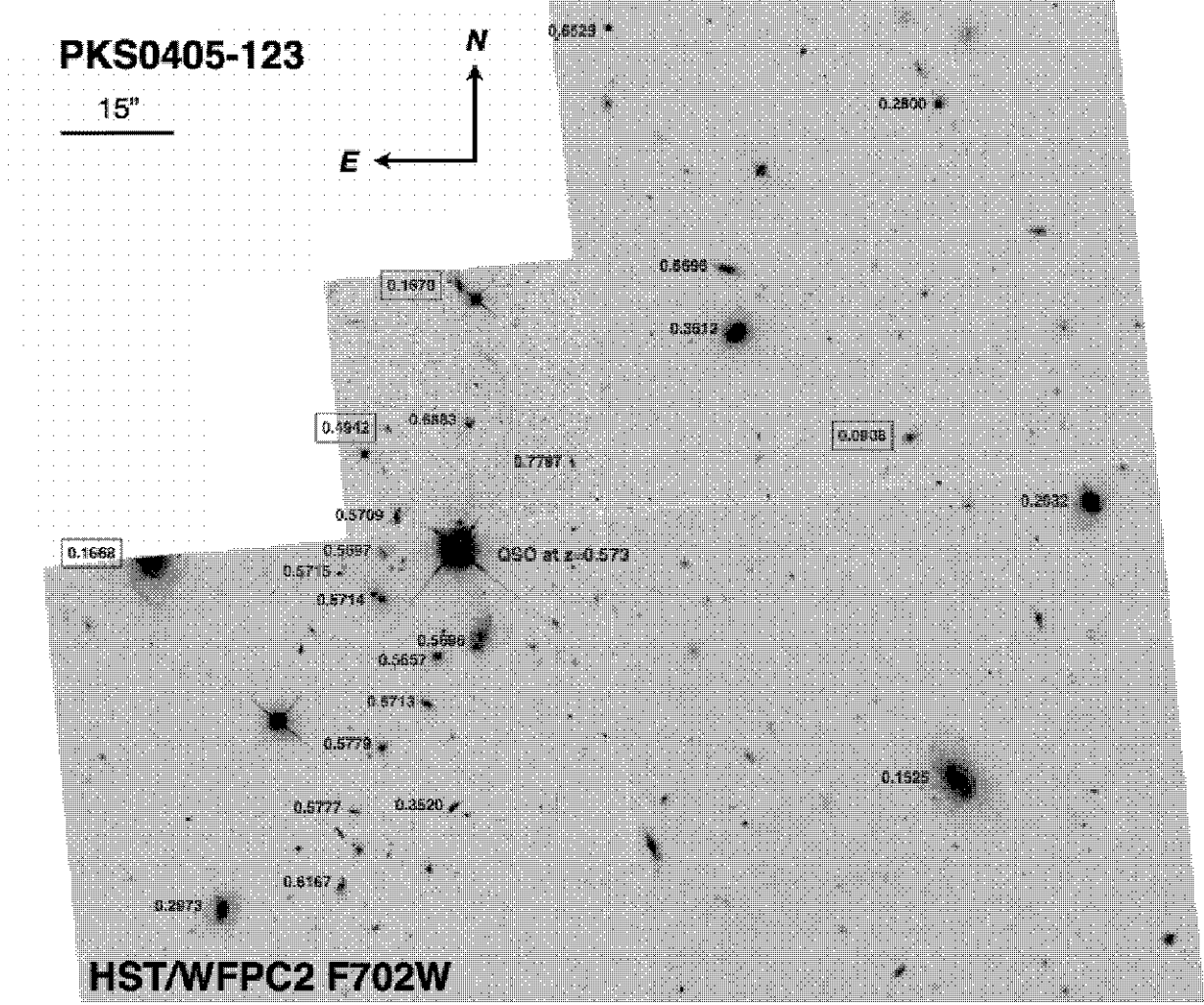


FIG. 9.— A combined HST image obtained using WFPC2 and the F702W filter. The image is roughly $2.7'$ on a side. Galaxies with known spectroscopic redshifts are indicated by their redshifts to the left. Blue values represent redshift measurements obtained by previous authors (Spinrad et al. 1993; Prochaska et al. 2006). Red values represent new redshifts obtained in our survey. Similar to Figure 8, galaxies with redshift coincident with known OVI absorbers ($|\Delta v| < 300 \text{ km s}^{-1}$) are marked by a rectangular box.

tion transitions (see also Tripp et al. 2008 for a brief discussion of this system). Narrow absorption due to the Si III $\lambda 1206$ transition is also detected, but only in three components. All four components of the Ly α absorption are saturated. We have performed a Voigt profile analysis to determine the column densities of individual components. The results are presented in Table 7, which lists from columns (2) through (9) the best-fit column density, Doppler parameter (b), and their associated uncertainties. Column (10) of Table 7 gives the total estimated column densities of individual transitions. Given the saturated profiles of the Ly α transition and relatively low resolution in the observation of Ly β , we place conservative limits for the underlying $N(\text{H I})$. The Si III components all appear to be very narrow and unresolved in the STIS echelle data. We estimate the column densities based on a fixed b value of $b = 2.4 \text{ km s}^{-1}$ that corresponds to gas of $\approx 10^4 \text{ K}$. The best-fit Voigt profiles are shown in the right panel of Figure 12 as smooth curves.

While the blue-shifted and redshifted components of Ly α and Ly β show nearly symmetric kinematic signatures (and possibly in the C III absorption as well) that are indicative

of an origin in expanding superbubble shells (see e.g. Bond et al. 2001 and Simcoe et al. 2002, although see also Kawata & Rauch 2007 who showed that such absorption features could also be produced by filamentary accretion onto a central galaxy or galaxy group), there exists a strong abundance gradient in Si III and O VI from $\Delta v = -158 \text{ km s}^{-1}$ to $\Delta v = +188 \text{ km s}^{-1}$ that suggests a significant variation in the underlying gas density (assuming a uniform background radiation field). Combining the optical morphology of the galaxy and the differential relative abundances of different ionization species indicates that the absorber is likely to originate in disrupted tidal tails as a result of a merger.

The nearest galaxy to the OVI absorber at $z = 0.28232$ (Tripp et al. 2008; Thom & Chen 2008a,b) has $R = 19.9$ and $\rho = 374 h^{-1}$ physical kpc, with a corresponding rest-frame R -band absolute magnitude of $M_R - 5 \log h = -20.3$. The galaxy spectrum is dominated by absorption features. Three more galaxies are found at $|\Delta v| < 300 \text{ km s}^{-1}$ from the absorber redshift, but they are over $\rho = 835 h^{-1} \text{ kpc}$ to $\rho = 2.0 h^{-1} \text{ Mpc}$ physical distances away.

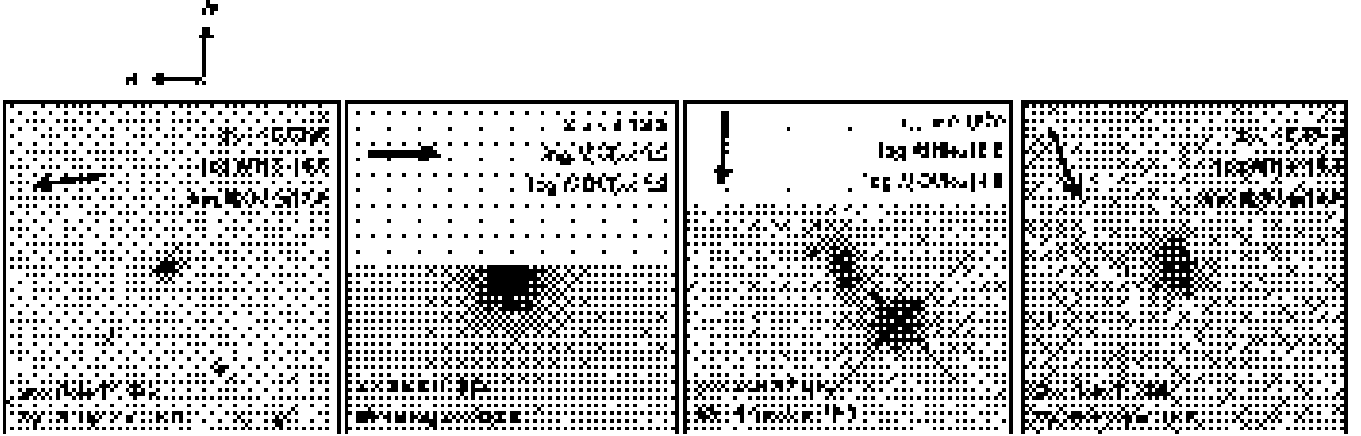


FIG. 10.— Optical morphologies of galaxies that are associated with known OVI absorbers along the sightline toward PKS 0405–123. Each panel is a subset of the combined WFPC2/F702W image presented in Figure 9. The absorbing galaxy is located at the center of each panel, which corresponds to roughly $25 h^{-1}$ physical kpc on a side at the redshift of the galaxy. The arrow in each panel indicates the direction toward the QSO sightline.

7. ANALYSIS

We have obtained a spectroscopic sample of galaxies in fields around three QSOs, for which ultraviolet echelle spectra from FUSE and HST/STIS are available for identifying intervening hydrogen Ly α and OVI absorbers. The galaxies span a broad range in the rest-frame R -band magnitude from $M_R - 5 \log h > -16$ to $M_R - 5 \log h < -22$ and a broad range in the projected physical distance from $\rho < 30 h^{-1}$ kpc to $\rho > 4 h^{-1}$ Mpc. We have shown in § 4.2 that the completeness of the spectroscopic survey is well understood and characterized by the angular selection function presented in Figure 6. Together with a complete sample of intervening Ly α and OVI absorbers found at $z = 0.01 - 0.5$ in these fields (§ 5 and Figure 7), the galaxy sample offers a unique opportunity for studying the origin of Ly α and OVI absorbers based on their cross-correlation amplitude with known galaxies, and for investigating the gas content in halos around galaxies.

7.1. The Galaxy–Absorber Cross-Correlation Functions

To quantify the origin of Ly α and OVI absorbers, we first measure the projected two-point galaxy auto-correlation func-

tion using a flux-limited sample that has been assembled from our spectroscopic survey. The flux-limited galaxy sample contains 670 spectroscopically identified intervening galaxies of $R \leq 22$ within $\Delta\theta = 11'$ of the background QSOs, 222 of which show absorption-line dominated spectral features. The median rest-frame R -band absolute magnitude of the 448 emission-line dominated galaxies is $\langle M_R \rangle - 5 \log h = -19.2$ (corresponding to $\approx 0.33 L_*$ for $M_R^* - 5 \log h = -20.44$ from Blanton et al. 2003), while the 222 absorption-line dominated galaxies have $\langle M_R \rangle - 5 \log h = -20.43$ (corresponding to $\approx L_*$). We calculate the projected two-point correlation function $\omega_{gg}(r_p)$ versus co-moving projected distance r_p , using the Landy & Szalay (1993) estimator

$$\omega_{gg}(r_p) = \frac{D_g D_g - 2 D_g R_g + R_g R_g}{R_g R_g}, \quad (1)$$

where D_g represents the input galaxy sample and R_g represents a random galaxy sample. The random galaxy sample is generated following the completeness function presented in Figure 6 for each field. To minimize possible counting noise introduced by the random galaxy sample, we have produced a random galaxy sample per field that is a factor of ten

TABLE 5
AN EXAMPLE OF THE PHOTOMETRIC AND SPECTROSCOPIC CATALOG OF OBJECTS IN THE FIELD AROUND PKS0405–123^a

ID (1)	RA(J2000) (2)	Dec(J2000) (3)	$\Delta\alpha$ ($''$) (4)	$\Delta\delta$ ($''$) (5)	$\Delta\theta$ ($''$) (6)	ρ (h^{-1} kpc) (7)	R (8)	z_{spec} (9)	Type ^b (10)	M_R $-5 \log h$ (11)
00071	04:08:33.10	-12:10:48.0	655.0	48.7	656.8	-1.00	21.340 ± 0.110	-1.0000	0	0.00
00078 ^c	04:08:32.80	-12:13: 9.0	650.5	-92.3	657.0	2980.30	20.510 ± 0.090	0.5639	1	-22.03
00089	04:08:32.50	-12:13:42.0	646.0	-125.3	658.1	-1.00	20.470 ± 0.080	-1.0000	0	0.00
00107	04:08:32.10	-12:14:17.0	640.2	-160.3	659.9	-1.00	19.740 ± 0.070	-1.0000	0	0.00
00108	04:08:32.30	-12:11:06.0	643.2	30.7	643.9	-1.00	21.230 ± 0.100	-1.0000	0	0.00
00114	04:08:32.20	-12:10:39.0	641.8	57.7	644.3	-1.00	21.290 ± 0.090	-1.0000	0	0.00
00120	04:08:32.00	-12:09:42.0	638.9	114.7	649.1	-1.00	16.970 ± 0.060	-1.0000	0	0.00
00123	04:08:31.80	-12:12:32.0	635.8	-55.3	638.2	-1.00	18.090 ± 0.060	-1.0000	0	0.00
00129	04:08:31.70	-12:14:01.0	634.3	-144.3	650.5	-1.00	20.810 ± 0.090	-1.0000	0	0.00
00138	04:08:31.40	-12:10:44.0	630.0	52.7	632.2	-1.00	17.290 ± 0.060	-1.0000	0	0.00
00142 ^c	04:08:32.00	-12:14:10.0	638.7	-153.3	656.8	2981.03	20.890 ± 0.090	0.5645	2	-20.86
00144	04:08:31.20	-12:13:59.0	627.0	-142.3	642.9	-1.00	21.320 ± 0.090	-1.0000	0	0.00
00145	04:08:31.20	-12:11:14.0	627.1	22.7	627.5	-1.00	17.570 ± 0.060	-1.0000	0	0.00
00149	04:08:31.00	-12:14:55.0	624.0	-198.3	654.8	-1.00	21.580 ± 0.120	-1.0000	0	0.00
00153	04:08:31.00	-12:13:02.0	624.1	-85.3	629.9	-1.00	21.600 ± 0.110	-1.0000	0	0.00
00162	04:08:31.00	-12:11:01.0	624.2	35.7	625.2	-1.00	21.890 ± 0.130	-1.0000	0	0.00
00163	04:08:30.70	-12:13:09.0	619.7	-92.3	626.5	-1.00	21.370 ± 0.100	-1.0000	0	0.00
00165	04:08:30.80	-12:11:30.0	621.2	6.7	621.2	-1.00	17.600 ± 0.060	-1.0000	0	0.00
00169	04:08:30.30	-12:15:00.0	613.7	-203.3	646.5	-1.00	16.240 ± 0.060	-1.0000	0	0.00
00174	04:08:30.60	-12:10:56.0	618.3	40.7	619.6	-1.00	19.140 ± 0.070	-1.0000	0	0.00
00175	04:08:30.80	-12:08:27.0	621.3	189.7	649.6	-1.00	21.220 ± 0.090	-1.0000	0	0.00
00179	04:08:30.60	-12:11:14.0	618.3	22.7	618.7	-1.00	21.590 ± 0.110	-1.0000	0	0.00
00190	04:08:30.60	-12:08:09.0	618.4	207.7	652.3	-1.00	21.760 ± 0.120	-1.0000	0	0.00
00191	04:08:30.00	-12:13:17.0	609.4	-100.3	617.6	-1.00	21.980 ± 0.130	-1.0000	0	0.00
00203	04:08:29.60	-12:13:26.0	603.5	-109.3	613.4	-1.00	20.830 ± 0.080	-1.0000	0	0.00
00209	04:08:29.80	-12:09:00.0	606.6	156.7	626.5	-1.00	19.400 ± 0.070	-1.0000	0	0.00
00210	04:08:29.90	-12:08:04.0	608.1	212.7	644.2	-1.00	20.800 ± 0.090	-1.0000	0	0.00
00213	04:08:29.40	-12:15:16.0	600.5	-219.3	639.3	-1.00	21.170 ± 0.100	-1.0000	0	0.00
00214	04:08:29.50	-12:11:19.0	602.2	17.7	602.4	-1.00	21.560 ± 0.110	-1.0000	0	0.00
00221 ^d	04:08:29.00	-12:13:28.0	594.7	-111.3	605.1	2079.39	19.400 ± 0.070	0.3466	1	-20.41

^a A complete catalog is available electronically at http://lambda.uchicago.edu/public/cat/cat_0405.html. The Object ID, coordinates, and R -band photometry are adopted from Prochaska et al. (2006).

^b Spectral type of the galaxy: 1 \rightarrow absorption-line dominated and 2 \rightarrow emission-line dominated.

^c New Spectroscopic redshifts obtained in our survey.

^d Spectroscopic redshifts published in Prochaska et al. (2006).

larger than the true galaxy sample. The two-point function is then calculated by counting the appropriate $D_g D_g$, $D_g R_g$, and $R_g R_g$ pairs within different r_p intervals, from $r_p < 250 h^{-1}$ kpc, to $r_p = 250 - 800 h^{-1}$ kpc, to $r_p = 800 - 1500 h^{-1}$ kpc, and to $r_p = 1.5 - 3 h^{-1}$ Mpc.

We present in panel (a) of Figure 13 the auto-correlation functions intergrated over $40 h^{-1}$ co-moving Mpc in redshift space for all galaxies (open circles), absorption-line dominated galaxies (open triangles), and emission-line dominated galaxies (open squares) in the flux-limited sample. Error-bars represent poisson counting uncertainties¹². These data points for each of these subsamples are also repeated in panels (b), (c), and (d), respectively, to be compared with their corresponding galaxy-absorber cross-correlation functions. Panel (a) of Figure 13 confirms that absorption-line dominated galaxies indeed cluster more strongly than emission-line dominated galaxies. The observed clustering amplitude of absorption-line dominated galaxies in our sample is comparable to what is found by Zehavi et al. (2005) for SDSS

galaxies of $M_R - 5 \log h < -19$ at $z \sim 0.1$. The stronger clustering amplitude indicates that on average these absorption-line galaxies originate in higher overdensity regions and presumably more massive dark matter halos.

Next, we measure the projected two-point galaxy-absorber cross-correlation function using the flux-limited galaxy sample discussed above and the absorber catalogs discussed in § 5. We exclude absorbers that are within $\Delta v = 3000 \text{ km s}^{-1}$ of the background QSO to reduce contaminations due to QSO associated absorbers. There are 195 Ly α absorbers and 15 OVI absorbers included in our analysis. We calculate the projected two-point cross-correlation function $\omega_{ga}(r_p)$ versus co-moving projected distance r_p between galaxies and absorbers, using the Landy & Szalay (1993) estimator

$$\omega_{ga}(r_p) = \frac{D_g D_a - D_g R_a - R_g D_a + R_g R_a}{R_g R_a}, \quad (2)$$

where D_g and D_a represent the input galaxy and absorber samples, and R_g and R_a represent random galaxy and absorber samples. We have produced random Ly α and OVI absorber catalogs for each field, assuming a flat absorber selection function in the redshift interval between $z = 0.01$ and z_{QSO} . The random absorber catalogs are also ten times larger than the true absorber catalogs. The two-point cross-correlation function is then calculated by counting the appropriate $D_g D_a$, $D_g R_a$, $R_g D_a$, and $R_g R_a$ pairs within the same r_p intervals of the auto-correlation function calculation.

¹² We note that on small scales ($r_p \lesssim 1 h^{-1}$ Mpc) the correlation amplitude is dominated by satellite galaxies (e.g. Zheng et al. 2007). Errors in the measured clustering signals on these scales are expected to be roughly poisson counting errors. On larger scales, however, field-to-field variations are expected to dominate the errors in the observed clustering signals and the reported poisson errors represent a lower limit to the true uncertainties. Given that our survey covers only three QSO fields, we are unable to evaluate the uncertainties due to field-to-field variations using a jackknife method.

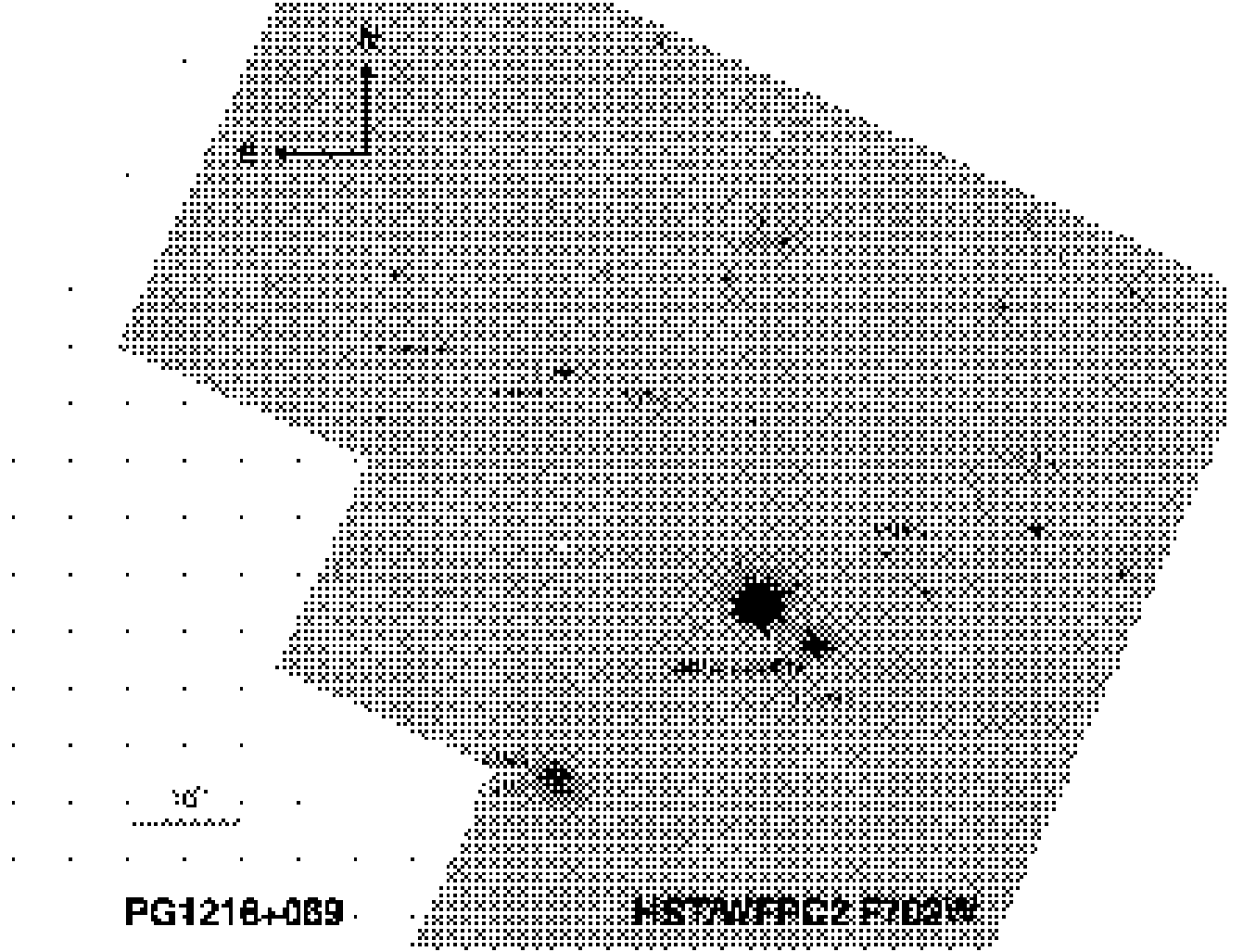


FIG. 11.— A combined HST image obtained using WFPC2 and the F702W filter. The image is roughly $2.7'$ on a side. Galaxies with known spectroscopic redshifts are indicated by their redshifts to the left. Known redshifts obtained prior to our survey are marked in blue (Chen et al. 2001a). Red values represent our own measurements. The galaxy with a redshift coincident with the O VI absorber at $z = 0.1236$ is marked by a rectangular box. The compact source at NE of the galaxy turns out to be a star. No additional foreground galaxies have been found at $\rho < 200 h^{-1}$ kpc.

Panels (b), (c), and (d) of Figure 13 show the galaxy- $\text{Ly}\alpha$ absorber and galaxy-OVI absorber cross-correlation functions integrated over $40 h^{-1}$ co-moving Mpc in redshift space. Comparisons between galaxy-absorber cross-correlation and galaxy auto-correlation functions of different galaxy type show four interesting features.

First, while both strong and weak $\text{Ly}\alpha$ absorbers exhibit on average weaker clustering amplitudes than the galaxies as a whole (solid points in panel b), strong $\text{Ly}\alpha$ absorbers of $\log N(\text{HI}) \geq 14$ appear to exhibit a comparable clustering amplitude on large scales of $r_p = 0.25 - 3 h^{-1}$ Mpc and a higher clustering amplitude on small scales of $r_p \leq 250 h^{-1}$ kpc with the emission-line dominated galaxies (solid points with solid errorbars panel c). The comparable clustering signal on large scales indicates that strong $\text{Ly}\alpha$ absorbers and emission-line galaxies share common halos. The higher galaxy-absorber cross-correlation signal relative galaxy auto-correlation signal on small scales is understood if the gas covering fraction is high in halos around these galaxies. Taking into account previous findings of Chen et al. (1998; 2001a), we conclude that

emission-line dominated galaxies are surrounded by extended gas of nearly unity covering fraction and that strong $\text{Ly}\alpha$ absorbers primarily probe extended gaseous halos around young star-forming galaxies.

Second, these strong $\text{Ly}\alpha$ absorbers exhibit on average ≈ 6 times weaker amplitude with the absorption-line dominated galaxies (solid points with solid errorbars panel d) at all separations of $r_p < 3 h^{-1}$ Mpc. The weaker clustering amplitude between strong $\text{Ly}\alpha$ absorbers and absorption-line dominated galaxies is qualitatively consistent with the clustering amplitude of Mg II absorbers and luminous red galaxies (LRGs) found by Gauthier et al. (2009) using a flux-limited LRG sample. It suggests that the incidence of strong $\text{Ly}\alpha$ absorbers is very low around these absorption-line dominated galaxies.

Third, weak $\text{Ly}\alpha$ absorbers of $\log N(\text{HI}) < 13.5$ exhibit only a weak clustering signal to galaxies of all type at separations $r_p < 3 h^{-1}$ Mpc (solid points with dotted errorbars in Figure 13). The weak clustering amplitude indicates that the majority of these weak absorbers do not share the same dark matter halos as the galaxies. This result extends the finding of Grogin & Geller (1998) to $\lesssim 0.3 L_*$ galaxies that weak

TABLE 6
AN EXAMPLE OF THE PHOTOMETRIC AND SPECTROSCOPIC CATALOG OF OBJECTS IN THE FIELD AROUND PG1216+069^a

ID (1)	RA(J2000) (2)	Dec(J2000) (3)	$\Delta\alpha$ ($''$) (4)	$\Delta\delta$ ($''$) (5)	$\Delta\theta$ ($''$) (6)	ρ (h^{-1} kpc) (7)	B (8)	R (9)	I (10)	z_{spec} (11)	Type ^b (12)	M_R $-5 \log h$ (13)
00539	12:18:48.159	+06:32:41.11	-484.7	-358.0	602.6	-1.00	18.723 \pm 0.023	16.923 \pm 0.005	16.654 \pm 0.005	-1.0000	0	0.00
01375	12:19:20.821	+06:27:37.63	0.9	-657.5	657.5	2023.15	21.500 \pm 0.014	20.237 \pm 0.005	19.765 \pm 0.006	0.2943	2	-19.79
01419	12:19:21.951	+06:27:38.90	17.7	-656.2	656.4	-1.00	21.148 \pm 0.012	18.744 \pm 0.002	17.645 \pm 0.001	-1.0000	0	0.00
01454	12:19:21.826	+06:27:48.01	15.8	-647.1	647.3	-1.00	22.316 \pm 0.019	21.763 \pm 0.015	21.491 \pm 0.021	-1.0000	0	0.00
01567	12:19:14.802	+06:27:54.42	-88.4	-641.2	647.3	2551.46	22.493 \pm 0.026	21.123 \pm 0.010	20.820 \pm 0.012	0.4328	2	-19.89
01591	12:19:13.861	+06:27:58.57	-102.4	-637.2	645.3	-1.00	23.090 \pm 0.046	20.541 \pm 0.006	19.378 \pm 0.004	-1.0000	0	0.00
01610	12:19:27.817	+06:27:50.45	104.6	-644.3	652.7	1357.74	20.959 \pm 0.015	19.128 \pm 0.004	18.510 \pm 0.004	0.1753	2	-19.67
01619	12:19:10.432	+06:27:56.42	-153.2	-639.5	657.6	-1.00	22.830 \pm 0.040	21.748 \pm 0.019	21.337 \pm 0.024	-1.0000	0	0.00
01621	12:19:24.357	+06:27:49.33	53.3	-645.6	647.8	2044.82	21.010 \pm 0.011	19.615 \pm 0.004	19.123 \pm 0.004	0.3054	2	-20.50
01693	12:19:28.263	+06:27:56.16	111.2	-638.6	648.2	-1.00	22.168 \pm 0.038	20.307 \pm 0.009	19.929 \pm 0.012	-1.0000	0	0.00
01740	12:19:27.316	+06:27:58.82	97.1	-636.0	643.4	-1.00	18.688 \pm 0.002	17.676 \pm 0.001	17.384 \pm 0.001	-1.0000	0	0.00
01785	12:19:26.316	+06:28:10.08	82.3	-624.9	630.2	-1.00	22.555 \pm 0.034	20.485 \pm 0.006	19.921 \pm 0.005	-1.0000	0	0.00
01794	12:19:12.163	+06:28:13.40	-127.6	-622.5	635.5	-1.00	22.901 \pm 0.029	21.660 \pm 0.013	21.428 \pm 0.020	-1.0000	0	0.00
01814	12:19:23.459	+06:27:58.51	40.0	-636.6	637.8	1979.71	21.963 \pm 0.028	20.423 \pm 0.009	19.919 \pm 0.010	0.2981	2	-19.64
01819	12:19:18.003	+06:28:07.61	-41.0	-627.9	629.2	1953.51	22.342 \pm 0.034	20.752 \pm 0.010	20.270 \pm 0.012	0.2981	2	-19.31
01852	12:19:15.205	+06:28:10.43	-82.5	-625.3	630.7	2756.59	23.582 \pm 0.111	20.399 \pm 0.008	19.560 \pm 0.006	0.5220	1	-21.84
01875	12:19:25.887	+06:28:17.02	75.9	-618.0	622.6	-1.00	22.975 \pm 0.035	21.821 \pm 0.017	21.236 \pm 0.016	-1.0000	0	0.00
01897	12:19:32.437	+06:28:15.65	173.0	-618.9	642.6	-1.00	22.797 \pm 0.046	21.590 \pm 0.020	21.289 \pm 0.024	-1.0000	0	0.00
01898	12:19:09.029	+06:28:19.40	-174.1	-616.8	640.9	-1.00	23.362 \pm 0.065	21.496 \pm 0.015	20.783 \pm 0.015	-1.0000	0	0.00
01915	12:19:33.091	+06:28:20.09	182.7	-614.4	641.0	-1.00	23.848 \pm 0.101	21.792 \pm 0.019	21.147 \pm 0.017	-1.0000	0	0.00
01921	12:19:13.717	+06:28:24.51	-104.6	-611.4	620.3	-1.00	22.682 \pm 0.022	21.873 \pm 0.015	21.701 \pm 0.025	-1.0000	0	0.00
01972	12:19:17.545	+06:28:20.58	-47.8	-615.0	616.9	1746.19	22.692 \pm 0.045	21.316 \pm 0.016	20.763 \pm 0.020	0.2618	2	-18.43
01996	12:19:35.051	+06:28:26.57	211.7	-607.8	643.6	-1.00	22.038 \pm 0.018	21.173 \pm 0.010	20.940 \pm 0.014	-1.0000	0	0.00
02007	12:19:19.594	+06:28:27.37	-17.5	-608.1	608.4	-1.00	22.915 \pm 0.042	19.955 \pm 0.004	18.404 \pm 0.002	-1.0000	0	0.00
02025	12:19:16.440	+06:28:31.24	-64.3	-604.5	607.9	2661.45	23.481 \pm 0.064	21.396 \pm 0.014	20.673 \pm 0.012	0.5237	2	-20.14
02028	12:19:13.644	+06:28:23.06	-105.7	-612.8	621.9	-1.00	21.271 \pm 0.016	20.161 \pm 0.008	19.790 \pm 0.010	-1.0000	0	0.00
02044	12:19:34.051	+06:28:29.44	196.9	-605.1	636.3	-1.00	23.178 \pm 0.052	21.980 \pm 0.022	21.772 \pm 0.031	-1.0000	0	0.00
02048	12:19:17.171	+06:28:25.84	-53.4	-609.8	612.2	-1.00	23.015 \pm 0.061	21.382 \pm 0.018	20.722 \pm 0.018	-1.0000	0	0.00
02108	12:19:37.598	+06:28:37.06	249.4	-597.2	647.2	-1.00	23.376 \pm 0.058	21.848 \pm 0.020	21.412 \pm 0.021	-1.0000	0	0.00
02111	12:19:13.945	+06:28:38.92	-101.3	-597.0	605.6	-1.00	21.601 \pm 0.011	20.708 \pm 0.006	20.529 \pm 0.010	-1.0000	0	0.00

^a A complete catalog is available electronically at http://lambda.uchicago.edu/public/cat_1216.html.

^b Spectral type of the galaxies: "1" indicates absorption-line dominated galaxies, "2" indicates emission-line dominated galaxies, and "0" indicates absence of spectra.

TABLE 7
COLUMN DENSITY MEASUREMENTS OF THE Ly α +OVI ABSORBER AT $z = 0.1242$ ALONG THE PG 1216+069 SIGHTLINE

Transition (1)	$\Delta v = -158 \text{ km s}^{-1}$		$\Delta v = -82 \text{ km s}^{-1}$		$\Delta v = +120 \text{ km s}^{-1}$		$\Delta v = +188 \text{ km s}^{-1}$		$\log N_{\text{tot}}$ (10)
	$\log N$ (2)	b (3)	$\log N$ (4)	b (5)	$\log N$ (6)	b (7)	$\log N$ (8)	b (9)	
HI 1215 ^a	> 14.8	...	> 15.0	...	> 15.0	...	14.3 \pm 0.1	12 \pm 2	> 15.5
Si III 1206 ^b	12.5 \pm 0.2	2.4	12.4 \pm 0.2	2.4	12.5 \pm 0.1	2.4	< 11.9	...	12.9 \pm 0.2
C III 977	13.6 \pm 0.2	17 \pm 7	13.7 \pm 0.1	25 \pm 5	13.3 \pm 0.1	26 \pm 10	13.4 \pm 0.1	36 \pm 12	14.1 \pm 0.2
O VI	14.5 \pm 0.2	13 \pm 4	14.0 \pm 0.1	24 \pm 9	13.8 \pm 0.2	29 \pm 17	14.1 \pm 0.1	42 \pm 13	14.8 \pm 0.2
1031, 1037 ^a									

^a See also Tripp et al. (2008).

^b The lines appear to be saturated. The reported column densities are estimated for the adopted Doppler parameter, $b = 2.4 \text{ km s}^{-1}$, that corresponds to gas of $\approx 10^4 \text{ K}$.

Ly α absorbers of $\log N(\text{HI}) < 13.5$ occur far more frequently in underdense regions in comparison to these dwarf galaxies. Clustering amplitudes measured at large separations of $r_p \approx 10 h^{-1} \text{ Mpc}$ are necessary to constrain the mean overdensities where these weak Ly α absorbers reside.

Finally, OVI absorbers exhibit similar clustering amplitudes as strong Ly α absorbers. Specifically, they show a comparable clustering amplitude (crosses in panel c of Figure 13) with emission-line galaxies on scales of $r_p = 0.25 - 1.5 h^{-1} \text{ Mpc}$ but a factor of ≈ 6 times lower (pentagon points in panel d of Figure 13) than absorption-line dominated galaxies. Despite large uncertainties, the differential clustering amplitudes suggest a direct association between OVI absorbers and star-

forming galaxies and a lack of physical connections between the majority of OVI absorbers and the gaseous halos around these massive, early-type galaxies.

We have also attempted to investigate possible dependence of the cross-correlation amplitude on the strength of OVI absorbers using a mark two-point correlation statistic (see e.g. Sheth et al. 2005). Applying the absorber column density as a mark, we could not distinguish whether such dependence is present. It appears that the sample size is still too small for such study to yield statistically significant results.

Nevertheless, the comparable clustering amplitude among emission-line galaxies, strong Ly α absorbers, and OVI absorbers is, however, difficult to interpret, because the num-

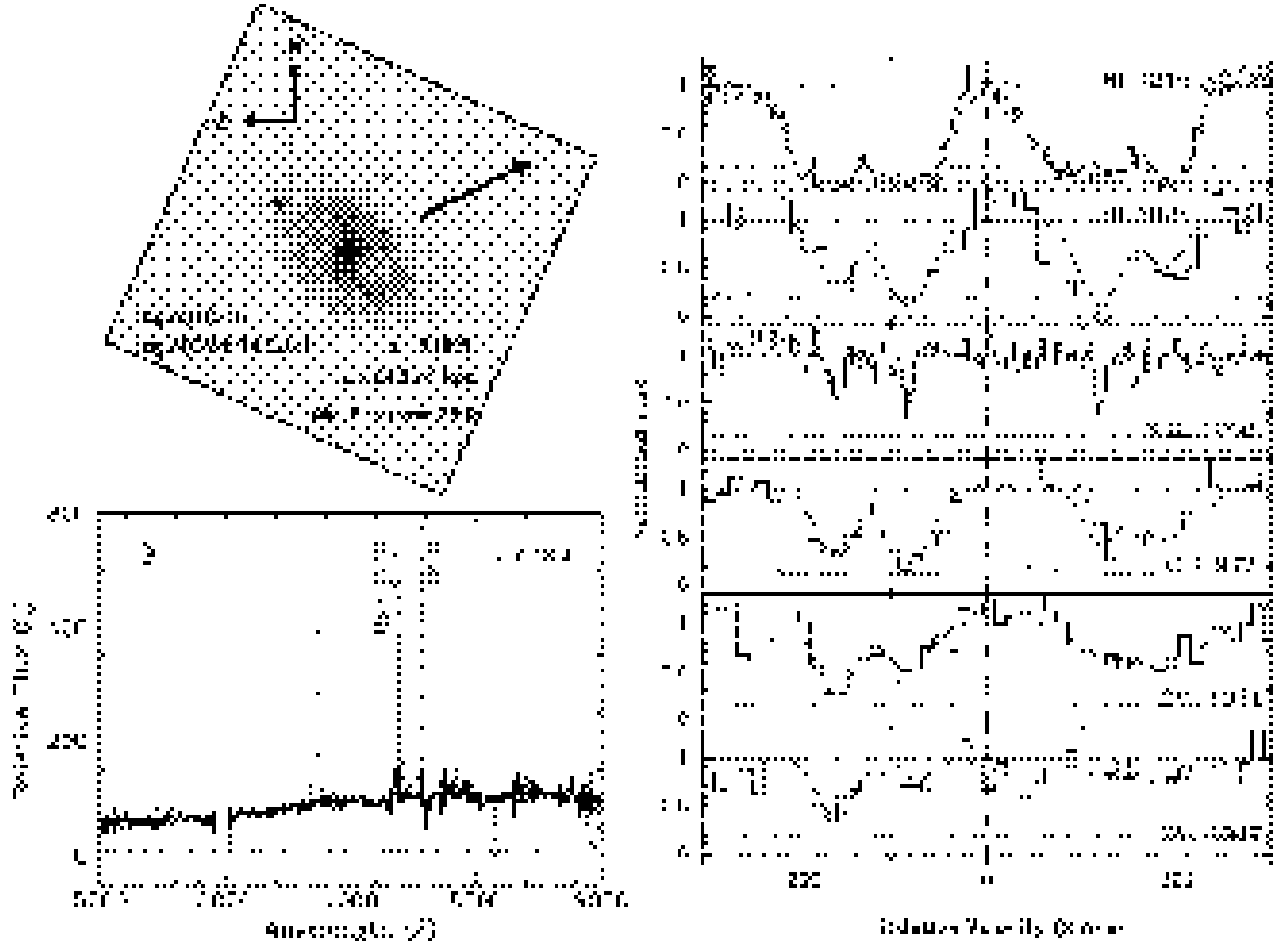


FIG. 12.— *Top Left*: Optical morphology of the OVI absorbing galaxy at $z = 0.1239$, as revealed in the WFPC2/F702W image. The image corresponds to roughly $25 h^{-1}$ kpc on a side at the galaxy redshift. The arrow indicates the direction toward the QSO sightline. *Bottom left*: The IMACS spectrum of the galaxy in the top panel, showing prominent emission features of H α , [N II], and [S II] (marked by dotted lines) that indicate an ISM metallicity comparable to solar. The weak H β line suggests the presence of substantial dust. The gap at 6000 \AA is due to a chip gap between IMACS CCDs. *Right*: Absorption profiles of neutral and ionic species found at $z = 0.1242$ (corresponding to zero velocity in the absorption profile). The spectra were obtained using HST/STIS with a spectral resolution of $\delta v \approx 6.8 \text{ km s}^{-1}$ (Thom & Chen 2008a) and FUSE with a spectral resolution of $\delta v \approx 30 \text{ km s}^{-1}$ (kindly provided by J. Scott; see also Scott et al. 2004). The 1- σ error array is represented by the thin histograms above the zero level. The zero-flux level and normalized continuum level are marked by the dash-dotted lines. The At least four distinct components are present in the H I, C III, and O VI absorption transitions. Narrow absorption due to the Si III $\lambda 1206$ transition is also detected, but only in three components. Smooth curves represent the best-fit model from a Voigt profile analysis.

ber density of OVI absorbers is found to be $n_{\text{OVI}} \approx 10 - 17$ per unit redshift interval per line of sight (e.g. Tripp et al. 2008; Thom & Chen 2008a) and the number density of strong Ly α absorbers is found to be $n_{\text{Ly}\alpha} \approx 25 - 30$ (Weymann et al. 1998; Dobrzycki et al. 2002). It shows that on average roughly half of the strong Ly α absorbers have associated OVI. We defer a more detailed discussion of this discrepancy to § 8.2.

7.2. Incidence and Covering Fraction of OVI Absorbing Gas Around Galaxies

The galaxy sample also allows us to examine the incidence and covering fraction of OVI absorbing gas around galaxies. We have identified a total of 20 foreground galaxies of $R \leq 22$ in our spectroscopic sample that occur at co-moving projected distances $r_p \leq 250 h^{-1}$ kpc from the lines of sight to-

ward HE 0226–4110, PKS 0405–123, and PG 1216+069. Six of the galaxies are absorption-line dominated galaxies and eight are “isolated” galaxies without additional neighboring galaxies found at $r_p \leq 250 h^{-1}$ kpc from the QSO sightline and within velocity offsets of $\Delta v \leq 300 \text{ km s}^{-1}$. The adopted search volume is typical of the halo size around L_* galaxies. Galaxies and absorbers that occur in this small volume are likely to share a common halo.

For each galaxy in this sample, we search for corresponding OVI absorption features in the available echelle spectra of the QSOs and measure the rest-frame absorption equivalent width $W(1031)$. In the absence of an absorption feature, we determine a $2\text{-}\sigma$ upper limit to $W(1031)$ for the galaxy. Figure 14 shows $W(1031)$ versus r_p for these galaxies of $R \leq 22$ in our sample. Emission-line dominated galaxies are marked by squares and absorption-line dominated galaxies are marked

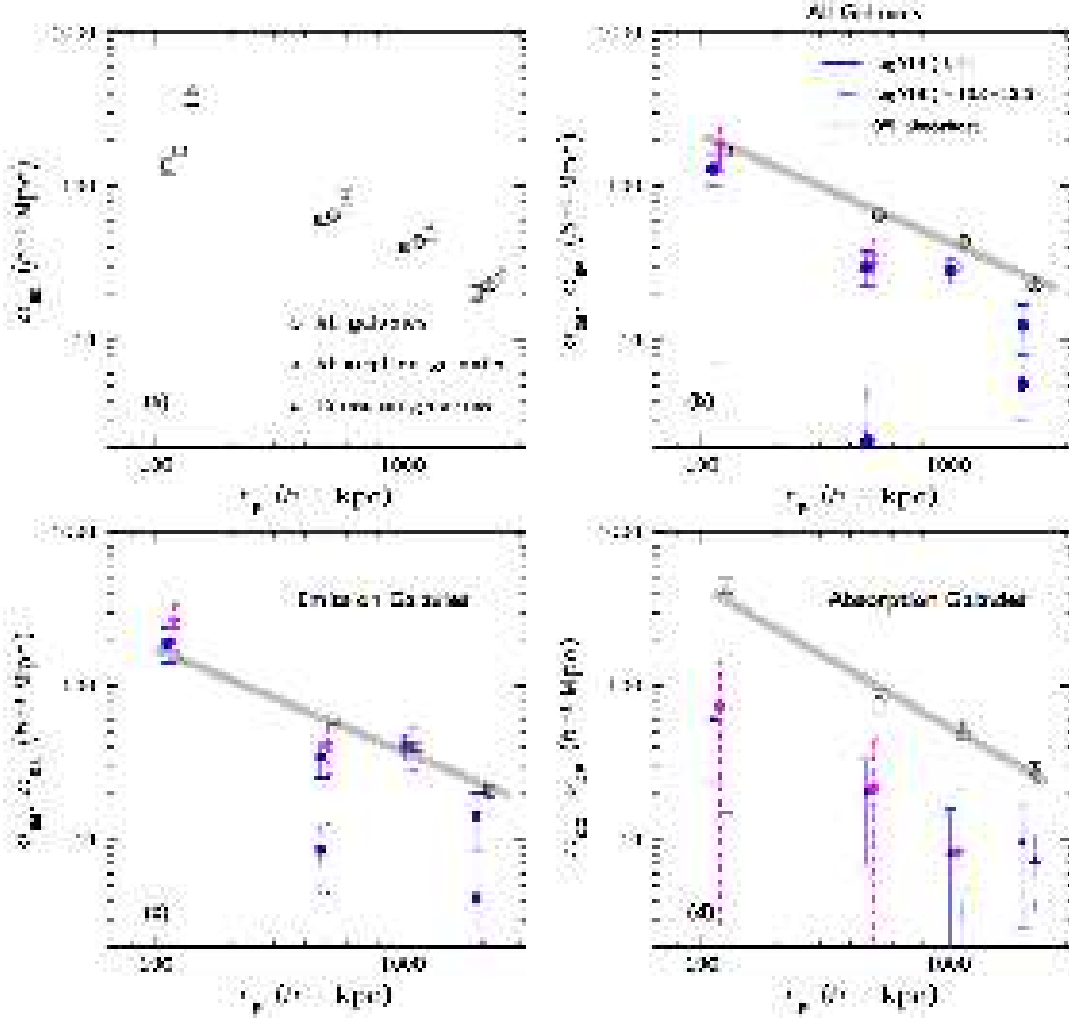


FIG. 13.— (a) Projected auto-correlation functions of galaxies in our flux-limited sample. Open circles represent the auto-correlation function including all galaxies; open triangles represent the auto-correlation function of emission-line dominated galaxies only; and open squares represent the auto-correlation function of absorption-line dominated galaxies only. We have applied a small offset in projected co-moving distance r_p to measurements for different subsamples for clarity. Each of the auto-correlation functions is repeated in panels (b), (c), and (d), respectively, for the corresponding type for direct comparison with the galaxy-absorber cross-correlation functions. (b) Projected galaxy-absorber cross-correlation functions, including all galaxies in the flux-limited sample. The solid points represent galaxy and $\text{Ly}\alpha$ absorber cross-correlation functions; points with solid errorbars are for strong $\text{Ly}\alpha$ absorbers of $\log N(\text{H I}) \geq 14$; points with dotted errorbars are for weak $\text{Ly}\alpha$ absorbers of $\log N(\text{H I}) = 12.5 - 13.5$. Stellar symbols with dashed errorbars represent the galaxy and OVI absorber cross-correlation function. The shaded line highlights the galaxy auto-correlation function to guide the comparisons with galaxy-absorber cross-correlation functions. (c) Similar to panel (b), but for emission-line dominated galaxies only. (d) Similar to panels (b) and (c), but for absorption-line dominated galaxies only.

by triangles. Arrows indicate the $2\text{-}\sigma$ upper limit in $W(1031)$ for galaxies that do not have an associated OVI absorber. For those galaxies with neighbors, we include only the galaxy at smallest r_p . These galaxies are marked by an additional open circle (indicating at least one neighboring galaxy is present at $r_p \leq 250 h^{-1}$ kpc from the absorber) in Figure 14.

It is clear that none of the absorption-line dominated galaxies in Figure 14 has a corresponding OVI absorber to a sensitive upper limit, consistent with the lower clustering amplitude seen in panel (d) of Figure 13. Considering only emission-line dominated galaxies in our sample, we find that nine of the 14 galaxies at $r_p \leq 250 h^{-1}$ kpc have an associated OVI absorber. This translates to a covering fraction of $\kappa \approx 64\%$ for OVI absorbing gas within $250 h^{-1}$ co-moving projected distance of star-forming galaxies. The covering fraction appears to be $\kappa \approx 100\%$ at $r_p \leq 100 h^{-1}$ kpc, as all four emission-line dominated galaxies have an associated

OVI absorber. The observed $\kappa \approx 64\%$ OVI covering fraction at $r_p \leq 250 h^{-1}$ kpc from emission-line galaxies is consistent with the known number density statistics of strong $\text{Ly}\alpha$ and OVI absorbers, but it further underscores the difficulty in interpreting the comparable clustering measurements presented in panel (c) of Figure 13.

We note that the OVI absorbing galaxy at $r_p = 72 h^{-1}$ in Figure 14 is the complex absorber at $z = 0.1242$ toward PG 1216+069. As shown in § 6.3 and Figure 12, the galaxy exhibits a disturbed morphology that suggests an on-going merger. It is therefore likely that this galaxy is located in a multiple galaxy environment. In addition, the only galaxy at $r_p < 100 h^{-1}$ that does not have a corresponding OVI absorber to a sensitive upper limit is an absorption-line dominated galaxy at $z = 0.2678$. At this redshift, an emission-line dominated galaxy of $R = 21.6$ at $r_p \approx 140 h^{-1}$ and an absorption-line dominated galaxy of $R = 18.6$ at $r_p = 251 h^{-1}$

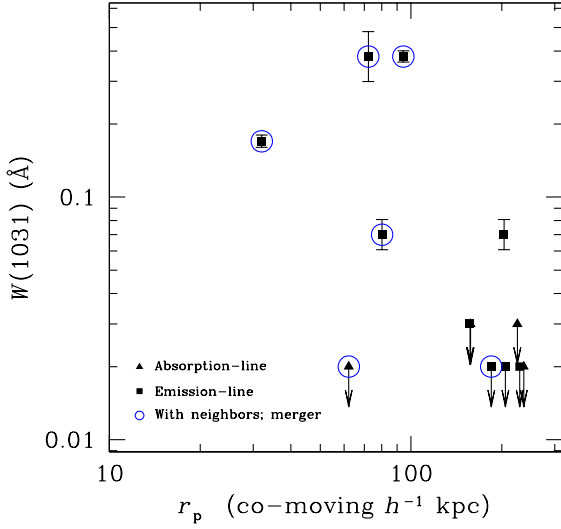


FIG. 14.— Observed OVI absorption strength for all galaxies of $R \leq 22$ found at $z = 0.01 - 0.5$ and co-moving projected distances $r_p \leq 250 h^{-1}$ kpc in the fields around HE0226–4110, PKS 0405–123, and PG 1216+069. Squares represent emission-line dominated galaxies, and triangles represent absorption-line dominated galaxies. Arrows indicate the $2\text{-}\sigma$ upper limit to the rest-frame 1031 Å absorption equivalent width for galaxies that do not have an associated OVI absorber. Note that there are two non-absorbing galaxies occur at $r_p \approx 157 h^{-1}$ kpc. Several galaxies are found to have at least one neighboring galaxy located within $r_p = 250 h^{-1}$ kpc and $|\Delta v| \leq 300$ km s $^{-1}$ from the absorber, in which cases we include only the closest galaxy in the plot. Points with open circles represent galaxies that either have additional neighboring galaxies or exhibit disturbed morphologies indicative of a merger event.

kpc are also found from the QSO sightline. Although our sample is still small and the results have large uncertainties because of systematic bias from possible field to field variations, it is interesting to find that star-forming galaxy “groups” at $r_p \lesssim 100 h^{-1}$ kpc appear to show a higher incidence of OVI absorbers.

8. DISCUSSION

Using a flux-limited ($R \leq 22$) sample of 670 intervening galaxies spectroscopically identified at $z < 0.5$ in fields around three QSOs, HE0226–4110, PKS 0405–123, and PG 1216+069, we have calculated the projected two-point correlation functions of galaxies and QSO absorption-line systems. Our analysis confirms early results of Chen et al. (2005; see also Figure 4 of Wilman et al. 2007) that strong Ly α absorbers of $\log N(\text{HI}) > 14$ share comparable clustering amplitude with emission-line dominated galaxies and that weak Ly α absorbers of $\log N(\text{HI}) \leq 13.5$ cluster only very weakly around galaxies. Combining the observed $\approx 100\%$ covering fraction around galaxies (Chen et al. 1998, 2001a) and the comparable clustering amplitude, we conclude that strong Ly α absorbers at $z < 0.5$ primarily probe extended gaseous halos around star-forming galaxies and that a large fraction of weak Ly α absorbers of $\log N(\text{HI}) \leq 13.5$ originate in low overdensity regions that occur more frequently than $\approx 0.3 L_*$ galaxies. The differential clustering amplitude of strong Ly α absorbers with different types of galaxies at projected co-moving distances $r_p \leq 250 h^{-1}$ kpc further indi-

cates that the incidence of strong Ly α absorbers is very low around absorption-line dominated galaxies.

We have also studied the correlation between galaxies and OVI absorbers. While our spectroscopic survey has uncovered multiple large-scale galaxy overdensities in the three fields, Figures 6&7 show that only two OVI absorbers (at $z = 0.0966$ toward PKS 0405–123 and at $z = 0.2823$ toward PG 1216+069) occur at the redshifts of these overdensities. An interesting result from the two-point correlation analysis is that while the majority of OVI absorbers do not probe the gaseous halos around massive, early-type galaxies, they appear to share common halos with emission-line dominated star-forming galaxies (and therefore with strong Ly α absorbers as well). The interpretation of the clustering analysis is, however, complicated by additional observations that the covering fraction of OVI absorbing gas is $\kappa \approx 64\%$ around emission-line dominated galaxies. While our sample is still small, this low gas covering fraction is qualitatively consistent with the observed difference in the number densities of strong Ly α and OVI absorbers. It indicates that only a subset of star-forming galaxies are associated with the observed OVI absorption features. The discrepancy between the observed clustering amplitude and covering fraction of OVI absorbers implies that additional variables need to be accounted for.

In this section, we review the known properties of individual OVI absorbing galaxies, and discuss the implications of our results on the origin of OVI absorbers and on the extended gaseous envelopes around galaxies.

8.1. The Properties of OVI Absorbing Galaxies

There are 13 OVI absorption systems (15 well-separated components) identified at $z = 0.017 - 0.495$ along the sightlines toward HE 0226–4110, PKS 0405–123, and PG 1216+069 (Tripp et al. 2008; Thom & Chen 2008a,b), including one at $z = 0.207$ with associated Ne VIII features (Savage et al. 2005). Our spectroscopic survey, together with previous searches in these fields, has uncovered 11 galaxies at projected co-moving distances of $r_p < 250 h^{-1}$ kpc and velocity offsets of $\Delta v \leq 300$ km s $^{-1}$ from six of the 13 OVI absorbers¹³. Although half of the OVI absorbers do not yet have an associated galaxy identified, this small sample of 11 galaxies allows us to examine the common properties of OVI absorbing galaxies, including the luminosity, galaxy environment, morphology, and spectral features.

First, the rest-frame R -band absolute magnitude of the galaxies associated with six OVI absorbers span a broad range from $M_R - 5 \log h = -15.4$ to $M_R - 5 \log h = -20.9$. Adopting the magnitude limit at which our spectroscopic survey is 100% complete, we further place a conservative upper limit on M_R for the underlying absorbing galaxies of six remaining OVI absorbers¹⁴. A summary of galaxies found in the vicinity of OVI absorbers is presented in Table 8, which lists from columns (2) through (11) the absorber redshift z_{abs} , the velocity centroid relative to z_{abs} of the OVI feature Δv_{OVI} ,

¹³ In the absence of peculiar velocity field, $\Delta v = \pm 300$ km s $^{-1}$ would correspond to a co-moving pathlength of $\pm 3.3 h^{-1}$ Mpc. Adopting the luminosity function of Blanton et al. (2003) and the two-point galaxy auto-correlation function of Zehavi et al. (2005), we estimate that the probability of finding a random galaxy of $L > 0.1 L_*$ at $r_p < 100 h^{-1}$ co-moving kpc due to large-scale overdensity is $\approx 3\%$. The probability increases to 20% for $r_p < 250 h^{-1}$ kpc.

¹⁴ We have excluded the OVI absorber at $z = 0.01746$ toward HE 0226–4110, because at this low redshift our spectroscopic survey area only covers $\approx 170 h^{-1}$ kpc co-moving radius of the absorber.

the OVI absorbing gas column density $N(\text{OVI})$, the rest-frame absorption equivalent width $W_{\text{rest}}(1031)$, the velocity centroid relative to z_{abs} of the H I feature Δv_{HI} , the H I absorbing gas column density $N(\text{HI})$, references of the absorber measurements, the projected co-moving distance r_p and absolute magnitude M_R of the galaxies, and references of the galaxy measurements. We find that while the known OVI absorbing galaxies exhibit a broad range of intrinsic luminosity, from $< 0.01 L_*$ to $\approx L_*$, a clear correlation between $N(\text{OVI})$ and M_R is absent.

At the same time, four of the six OVI absorbers that have known associated galaxies are surrounded by either a merging galaxy pair or by more than one galaxy in the small volume of $r_p < 250 h^{-1} \text{ kpc}$ and $\Delta v \leq 300 \text{ km s}^{-1}$. In contrast, deep spectroscopic surveys to search for the galaxies producing absorption features of low-ionization species such as Mg II $\lambda\lambda 2796, 2803$ have yielded $\lesssim 16\%$ of Mg II absorbers originating in multiple galaxy environment (e.g. Steidel et al. 1997). On the other hand, not all galaxy “groups” within a similar volume produce an associated OVI absorber in the spectrum of the background QSO. We have shown in § 7.2 that a group of three galaxies at $z \approx 0.268$ and a group of two galaxies at $z \approx 0.199$ within $r_p \leq 250 h^{-1} \text{ kpc}$ from the sightline toward HE 0226–4110 do not have an associated OVI absorber. The most luminous members of both groups exhibit absorption-line dominated spectral features (see e.g. the bottom panel of Figure 15). It appears that OVI originates preferentially in groups of gas-rich galaxies. A detailed investigation using a statistically representative sample of galaxy groups close to QSO sightlines is necessary to confirm this result (see Thom et al. 2009, in preparation).

Using available high-resolution images in the HST archive, we are also able to examine the detailed optical morphology of five galaxies in the sample of 11 OVI absorbing galaxies. Individual images presented in Figures 10 & 12 show that four of the galaxies (responsible for three OVI absorbers) exhibit disk-like morphology with mildly disturbed features on the edge. This asymmetric disk morphology suggests that tidal disruption may be in effect. The OVI absorbing galaxy at $z = 0.4942$ (right panel of Figure 10) appears to be a regular disk, although the available image depth is insufficient to reveal more details.

Finally, all but one of these 11 OVI absorbing galaxies show prominent emission-line features that suggest a range of ISM metallicity and star formation history. The exception is a galaxy at $z = 0.2077$ and projected co-moving distance $r_p = 238 h^{-1} \text{ kpc}$ from the sightline toward HE 0226–4110, which exhibits primarily absorption features in the spectrum (see Mulchaey & Chen 2009). The spectra of three OVI absorbing galaxies, one at $z = 0.0965$ and two at $z = 0.1670$ toward PKS 0405–123, have been published by previous authors (see Spinrad et al. 1993; Prochaska et al. 2006). The spectra of three galaxies identified for the OVI + Ne VIII absorber at $z = 0.207$ toward HE 0226–4110 are presented in Mulchaey & Chen (2009). Two of these galaxies show emission-line dominated spectral features. The spectrum of the OVI absorbing galaxy at $z = 0.1239$ toward PG 1216+069 is presented in Figure 12. It exhibits strong emission features due to H α , [N II], and [S II] that imply roughly solar metallicity in the ISM. In the top four panels of Figure 15, we present the spectra of four additional OVI absorbing galaxies identified in our survey, three of which are for the OVI absorber at $z = 0.0918$ toward PKS 0405–123 and one for the OVI ab-

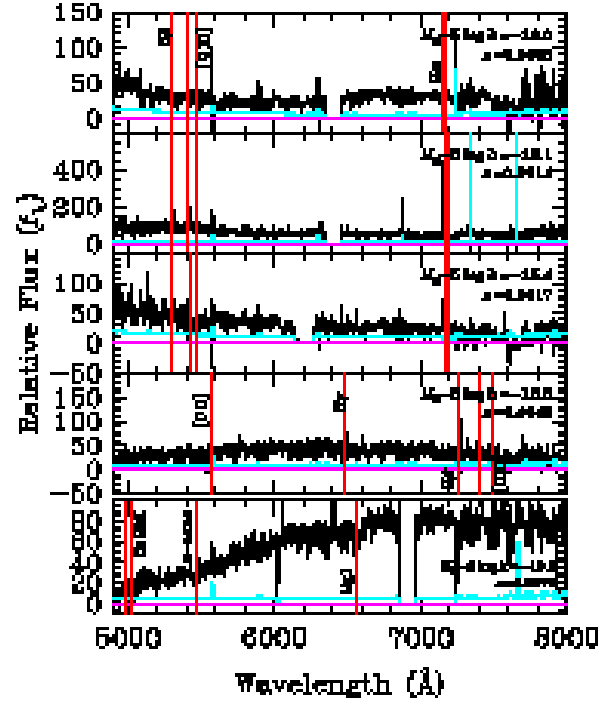


FIG. 15.— Spectra and the associated error arrays of four new OVI absorbing galaxies identified in our survey (top four panels), three of which are for the OVI absorber at $z = 0.0918$ toward PKS 0405–123 and one for the OVI absorber at $z = 0.4951$ along the same sightline. The rest-frame absolute magnitude M_R and the best-fit redshift of each galaxy are given in the upper-right corner of each panel. Dotted lines indicate the emission features found at the best-fit galaxy redshift. For comparison, we have included in the bottom panel the spectrum of an absorption-line dominated galaxy at $z = 0.2678$ and $r_p = 62 h^{-1} \text{ co-moving kpc}$ from the sightline toward HE 0226–4110. The galaxy has $M_R - 5 \log h = -19.9$ and does not have a corresponding OVI absorber to a $2\text{-}\sigma$ upper limit of $W(1031) < 0.02 \text{ \AA}$.

sorber at $z = 0.4951$ along the same sightline. Emission line features, such as H β and [O III], are present in all four galaxies. While the OVI absorbing galaxy at $z = 0.4942$ exhibits Balmer absorption series that implies a post-starburst nature, the lack of [N II] emission features together with the presence of strong H α emission in the three OVI absorbing galaxies at $z = 0.091$ places $2\text{-}\sigma$ upper limits to the ISM metallicity at $\approx 10\%$ to 30% of solar values. In contrast to the spectral features of OVI absorbing galaxies, we include in the bottom panel of Figure 15 the spectrum of an absorption-line dominated galaxy at $z = 0.2678$ and $r_p = 62 h^{-1} \text{ co-moving kpc}$ from the sightline toward HE 0226–4110. The galaxy has $M_R - 5 \log h = -19.9$ and does not have a corresponding OVI absorber to a $2\text{-}\sigma$ upper limit of $W(1031) < 0.02 \text{ \AA}$.

Excluding the OVI absorber at $z = 0.01746$ toward HE 0226–4110 for which our galaxy survey does not cover beyond $160 h^{-1} \text{ kpc}$, we note that four of the five strong OVI absorbers with $\log N(\text{OVI}) \geq 14$ have been identified with galaxies at $r_p < 250 h^{-1} \text{ kpc}$ and $\Delta v \leq 300 \text{ km s}^{-1}$, while only two of the seven weaker OVI absorbers with $\log N(\text{OVI}) < 14$ have been identified with galaxies at $r_p < 250 h^{-1} \text{ kpc}$ and $\Delta v \leq 300 \text{ km s}^{-1}$. Given the small sample size, we cannot

TABLE 8
SUMMARY OF GALAXIES IN THE VICINITY OF OVI ABSORBERS AT $z < 0.5^a$

Sightline (1)	z_{abs} (2)	Absorbers						Galaxies		
		Δv_{OVI} (km s $^{-1}$) (3)	$\log N(\text{OVI})$ (4)	$W_{\text{rest}}(1031)$ (mÅ) (5)	Δv_{HI} (km s $^{-1}$) (6)	$\log N(\text{HI})$ (7)	Reference ^c (8)	r_p (h^{-1} kpc) (9)	M_R^b −5 log h (10)	Reference ^c (11)
HE 0226–4110	0.01746	0	13.6 ± 0.1	40 ± 10	0	13.28 ± 0.06	(1)	
	0.20701	0	14.37 ± 0.03	169 ± 15	−24	15.06 ± 0.04	(2)	32.0	−17.2	(3)
					+5	14.89 ± 0.05	(2)	92.3	−18.9	(3)
								238.1	−18.9	(3)
	0.32639	0	13.6 ± 0.2	43 ± 8	0	< 12.5	(4)	...	> −17.3	(3)
	0.34034	0	13.9 ± 0.1	62 ± 7	0	13.6 ± 0.1	(4)	...	> −17.4	(3)
	0.35529	0	13.7 ± 0.1	46 ± 8	0	13.6 ± 0.2	(4)	...	> −17.5	(3)
	0.09180	+20	13.80 ± 0.04	73 ± 8	0	14.52 ± 0.04	(5)	80.2	−16.0	(3)
PKS 0405–123								101.2	−16.1	(3)
								228.5	−15.4	(3)
	0.09658	0	13.7 ± 0.2	71 ± 9	0	14.65 ± 0.05	(5)	203.5	−18.2	(6)
	0.16710	0	14.78 ± 0.07	361 ± 41	0	16.45 ± 0.05	(5),(7)	94.3	−20.9	(8)
								79.1	−18.1	(8)
	0.18291	−87	13.7 ± 0.2	42 ± 13	−82	14.90 ± 0.05	(4),(5)	...	> −18.9	(3)
		0	14.0 ± 0.2	65 ± 15	0	14.1 ± 0.1	(4),(5)	
	0.36332	0	13.5 ± 0.1	30 ± 5	0	13.6 ± 0.1	(4),(5)	...	> −20.6	(3)
	0.49510	0	14.5 ± 0.1	213 ± 16	0	14.3 ± 0.2	(4),(5),(9)	114.9	−18.8	(3)
	0.12420	−158	14.5 ± 0.2	225 ± 25	−158	> 14.8	(3)	72.2	−20.0	(3)
PG 1216+069		−82	14.0 ± 0.1		−82	> 15.0	(3)	
		+120	13.8 ± 0.2	194 ± 28	+120	> 15.0	(3)	
		+188	14.1 ± 0.1		+188	14.3 ± 0.1	(3)	
	0.28232	0	13.4 ± 0.2	26 ± 6	0	16.70 ± 0.04	(4),(10)	...	> −19.9	(3)

^aGalaxies are found at $r_p \leq 250 h^{-1}$ projected co-moving kpc and $\Delta v \leq 300 \text{ km s}^{-1}$.

^bIn cases where no absorbing galaxies have been found, we place a conservative upper limit for M_R based on the R -band threshold that corresponds to a 100% completeness out to $\Delta \theta < 2'$ in our spectroscopic survey. The magnitude thresholds are $R = 23$ for the field around HE 0226–4110, and $R = 20$ for the other two fields.

^c(1) Lehner et al. (2006); (2) Savage et al. (2005); (3) This work; (4) Thom & Chen (2008b); (5) Prochaska et al. (2004); (6) Prochaska et al. (2006); (7) Chen & Prochaska (2000); (8) Spinrad et al. (1993); (9) Howk et al. (2009); (10) Tripp et al. (2008).

rule out possible correlations between absorber strengths and galaxy properties or the possibility that some of the weaker OVI absorbers may originate in underdense IGM. For OVI absorbers that do not have galaxies found at $r_p < 250 h^{-1}$ kpc, we estimate the magnitude limit of the absorbing galaxies based on our survey depth and present these numbers in Column (9) of Table 8.

8.2. The Origin of OVI Absorption Systems

The galaxy–OVI absorber cross-correlation analysis presented in § 7.1 has clearly identified emission-line dominated galaxies to be principally responsible for the observed OVI absorbers, but the physical mechanism that distributes the metal-enriched gas to large galactic distances is unclear. Two competing scenarios to explain the origin of OVI absorbers in regions around emission-line galaxies are (1) starburst driven outflows (e.g. Heckman et al. 2001; Kawata & Rauch 2007; Oppenheimer & Davé 2009) and (2) satellite accretion (e.g. Wang 1993; Bournaud et al. 2004; Elmegreen et al. 2007). Given that these emission-line galaxies are presumably low-mass (given the sub- L_* nature) and star-forming (given the presence of strong emission lines), the strong correlation seems qualitatively consistent with the expectations of OVI originating in starburst outflows (c.f. Kawata & Rauch 2007; Oppenheimer & Davé 2009). On the other hand, satellite accretions or galaxy interactions are also expected to induce star formation (see e.g. Li et al. 2008). Here we examine whether additional insights for the origin of OVI absorbers can be gleaned based on known properties of the absorbing galaxies.

We have noted an apparent discrepancy between the observed partial covering fraction of OVI absorbing gas, $\kappa \approx$

64%, at projected co-moving distances $r_p \lesssim 250 h^{-1}$ kpc and the comparable clustering amplitudes of emission-line galaxies and OVI absorbers on scales $r_p \leq 1.5 h^{-1}$ Mpc. While the partial covering fraction indicates that not all emission-line galaxies contribute to the observed OVI absorber statistics, the comparable clustering amplitude suggests otherwise. Namely, every emission-line galaxy has a corresponding OVI absorber. Likewise, the comparable clustering amplitudes of OVI and strong Ly α absorbers also imply that the two absorber populations share common halos, but absorption-line surveys show that not all strong Ly α absorbers are accompanied by an OVI absorber (see e.g. Tables 3&8). Although both starburst outflows and tidal debris due to galaxy interactions may explain the observed partial covering fraction, it is not clear that they can both explain the comparable clustering amplitude at $r_p \lesssim 3 h^{-1}$ Mpc.

To understand these apparent discrepancies, we first note that the correlation amplitude on scales $r_p < 1 h^{-1}$ Mpc is dominated by galaxies that share common halos (e.g. Zheng et al. 2007; Tinker et al. 2007). The comparable clustering amplitudes of OVI and emission-line galaxies (and strong Ly α absorbers) found in our small sample from three QSO fields may be understood, if OVI absorbers arise preferentially in groups of emission-line galaxies. This hypothesis is supported by two features found in Figure 14. First, four of the five galaxy–OVI absorber pairs are indeed found in an environment of multiple emission-line galaxies. Second, only one of the four “isolated” emission-line galaxies has a corresponding OVI absorber. Available observations are indeed consistent with the expectations that OVI absorbers arise primarily in gas-rich galaxy groups. Taking into account the

mildly disturbed disk-like morphologies of OVI absorbing galaxies, we further argue that the OVI absorbers originate in tidal debris produced by galaxy interactions in a group or pair environment and that tidal interactions may be principally responsible for distributing chemically enriched gas to large galactic distances.

A larger sample is necessary to improve the uncertainties in the measurements of κ for both group/pair and “isolated” galaxies, and to address possible bias due to field to field variation. Extending the cross-correlation analysis to scales of $r_p \approx 10 h^{-1}$ Mpc is also necessary for constraining the mean halo mass of the absorbers based on their large-scale clustering amplitudes.

8.3. Extended Gas Around Galaxies

Previous studies have shown that luminous galaxies are surrounded by extended gaseous envelopes that may be probed by CIV and Mg II absorption transitions out to projected physical distances of $\rho \approx 100 h^{-1}$ kpc (e.g. Steidel et al. 1994; Chen et al. 2001b; Tinker & Chen 2008; Chen & Tinker 2008) and by strong Ly α absorption out to $\rho \approx 200 h^{-1}$ kpc (Lanzetta et al. 1995; Chen et al. 1998, 2001a). The covering fraction of extended gas probed by the presence of these transitions is found to be $> 80\%$. Our analysis extends these studies to OVI absorbing gas. We find extended OVI gas is indeed present around emission-line galaxies out to projected co-moving distance $r_p \approx 250 h^{-1}$ kpc (corresponding to a projected physical distance $\rho \approx 200 h^{-1}$ kpc at $z = 0.3$) with a mean covering fraction of $\kappa \approx 64\%$. While Ly α and Mg II absorption features are found to be progressively weaker in galaxies at larger impact parameters (Chen et al. 1998, 2001a; Chen & Tinker 2008), we find a lack of such correlation in either CIV (Chen et al. 2001b) or OVI (Figure 14). Including known OVI absorbing galaxies from Cooksey et al. (2008) and Lehner et al. (2009) further increases the scatter in the $W(1031)$ versus r_p distribution at $r_p < 250 h^{-1}$ kpc.

In a simple two-phase medium model, CIV and Mg II absorbers arise in photo-ionized cold clumps pressure-confined in a hot medium. The lack of correlation between CIV absorber strength and galaxy impact parameter can therefore be understood by higher gas pressure (and therefore reduced abundances of C³⁺) at smaller radii (e.g. Mo & Miralda-Escudé 1996). The same model cannot explain the presence of OVI around galaxies of a broad range of luminosity due to the high ionization potential. Instead, the mildly disturbed disk morphologies observed in OVI absorbing galaxies suggest that tidal debris in small groups or close galaxy pairs may be principally responsible for the observed OVI absorption features.

Additional insights may be learned from comparisons with known properties of the Milky Way halos. While exquisite details, including tidal streams, infalling clouds, and outflows, have been recorded for extended gas around the Milky Way (e.g. Sembach et al. 2003), applications of these observations for constraining models of galaxy growth has been limited due to a lack of knowledge for the distances to these Halo clouds. In contrast, observations of distant galaxy-absorbers pairs offer direct measurements of the distances between absorbing gas and star-forming regions, but the origin of the absorbing clouds (either due to accretion, outflow, or tidal stripping) is often more uncertain.

A systematic survey of OVI absorbers toward 100 extragalactic sources has yielded positive detections in the Galactic

thick disk and halo along 60–85% of these sightlines (Sembach et al. 2003). Because some of these detections are associated with known high velocity clouds at ≈ 10 kpc distances (e.g. Thom et al. 2008), the observed incidence of 60–85% represents an upper limit for the covering fraction of OVI absorbing gas over ~ 250 kpc radius to an external observer. This partial covering of OVI gas in the halo of the Milky Way, representing typical $\sim L_*$ galaxies in the nearby universe, is qualitatively consistent with the partial covering fraction found in our study for halos around distant sub- L_* galaxies. The lack of evidence for large-scale outflows in the Milky Way halo based on detections of OVI absorbers also appears to be consistent with our interpretation that the majority of OVI absorbers are not produced in starburst outflows around distant star-forming galaxies. A larger sample of galaxy–OVI absorber pairs that covers a broad range of impact parameters will allow a conclusive characterization of the nature of the OVI gas, which in turn will shed light for the halo gas content around the Milky Way.

Finally, our analysis has also shown that the majority of strong Ly α and OVI absorbers do not probe the gaseous halos around early-type galaxies. To study the warm-hot gas around early-type galaxies or galaxy groups would require a different probe.

9. SUMMARY

We have carried out a deep, wide-area survey of galaxies in fields around HE 0226–4110, PKS 0405–123, and PG 1216+069. The QSO fields are selected to have ultraviolet echelle spectra available from FUSE and HST/STIS. The high-resolution UV spectra have uncovered 195 Ly α absorbers of $\log N(\text{HI}) = 12.5 - 16.3$ and 13 OVI absorbers of $\log N(\text{OVI}) = 13.4 - 14.7$ (15 individual components) along the sightlines toward the background QSOs. The spectroscopic program has yielded redshift measurements for 1104 galaxies in three fields. The rest-frame R -band magnitudes of these galaxies range from $M_R - 5 \log h > -16$ to $M_R - 5 \log h \lesssim -22$. The projected physical distances of these galaxies range from $\rho < 30 h^{-1}$ kpc to $\rho > 4 h^{-1}$ Mpc. While our spectroscopic survey has uncovered multiple large-scale galaxy overdensities in the three fields, only two OVI absorbers (at $z = 0.0966$ toward PKS 0405–123 and at $z = 0.2823$ toward PG 1216+069) occur at the redshifts of these overdensities. Including previously found absorbing galaxies, we have collected a sample of ten galaxies that coincide with six OVI absorbers found along the three sightlines. Adopting our spectroscopic survey limit, we further place upper limits to the intrinsic luminosities of six remaining OVI absorbing galaxies that are still missing (three of these are expected to be fainter than $M_R - 5 \log h = -17.5$). Two of the fields, PKS 0405–123 and PG 1216+069, have high quality HST/WFPC2 images available that cover the $2' \times 2'$ area roughly centered at the QSO. These images also allow us to examine the optical morphologies of individual absorbing galaxies.

Combining various absorber and galaxy data, we have performed a cross-correlation study to understand the physical origin of Ly α and OVI absorbers and to constrain the properties of extended gas around galaxies. The main results of our study are summarize below.

1. Using a flux-limited sample of 670 foreground galaxies within $\Delta\theta = 11'$ of the QSO, we find based on a cross-correlation analysis that both strong Ly α absorbers of $\log N(\text{HI}) \geq 14$ and OVI absorbers exhibit a comparable clustering amplitude as emission-line dominated galaxies on

scales of $r_p < 3 h^{-1}$ co-moving Mpc. The clustering amplitudes of these absorbers are found to be ≈ 6 times lower than those of absorption-line dominated galaxies. At the same time, weak Ly α absorbers of $\log N(\text{HI}) < 13.5$ exhibit only a weak clustering signal to galaxies of all type. These findings confirm early results of Chen et al. (2005; see also Figure 4 of Wilman et al. 2007) that strong Ly α absorbers of $\log N(\text{HI}) \leq 14$ probe extended halos of emission-line dominated galaxies and that a large fraction of weak Ly α absorbers of $\log N(\text{HI}) \leq 13.5$ are likely to originate in low-overdensity regions that occur more frequently than $\approx 0.3 L_*$ galaxies.

2. OVI absorbers exhibit a similar behavior as strong Ly α absorbers. These absorbers also show a comparable clustering amplitude as emission-line galaxies but a factor of six lower clustering amplitude relative to absorption-line dominated galaxies on scales of $r_p \leq 3 h^{-1}$ Mpc. The results imply that the majority of OVI absorbers do not probe the gaseous halos around massive, early-type galaxies, and that they probe primarily halos around emission-line dominated star-forming galaxies.

3. Using a small sample of 20 $R \leq 22$ galaxies found at co-moving projected distances $r_p \leq 250 h^{-1}$ kpc from the lines of sight toward the three QSOs, we find that none of the absorption-line dominated galaxies in the sample has a corresponding OVI absorber to a sensitive upper limit of $W(1031) \lesssim 0.03 \text{ \AA}$, and that the covering fraction of OVI absorbing gas around emission-line dominated galaxies is $\kappa \approx 64\%$.

4. Four of the six OVI absorbers that have associated galaxies identified are surrounded by either a merging galaxy pair or by more than one galaxy in the small volume of $r_p < 250 h^{-1}$ kpc and $\Delta v \leq 300 \text{ km s}^{-1}$. On the other hand,

two galaxy “groups” found at $r_p \leq 250 h^{-1}$ kpc from a QSO sightline do not have an associated OVI absorber. A more detailed examination of galaxies in these latter two groups shows that the most luminous members of both groups exhibit absorption-line dominated spectral features, suggesting that OVI may originate preferentially in gas-rich galaxy groups.

5. Available high-resolution HST/WFPC2 images of five OVI absorbing galaxies show that these galaxies exhibit disk-like morphology with mildly disturbed features on the edge, suggesting that tidal disruption may be in effect.

JSM would like to acknowledge the visitor’s program at the Kavli Institute for Cosmological Physics, where part of the work presented here was completed. We thank helpful discussions with J. Tinker and C. Thom. We thank L. Matthews, M. Rauch, A. Kravtsov for helpful comments on an early version of the manuscript. We thank R. Simcoe and A. Bolton for assistance on obtaining part of the IMACS images presented in this paper and R. Marzke for helpful discussions on reducing and assembling geometrically distorted multi-CCD imaging data. We are grateful to D. Kelson and G. Walth for assistance on the reduction of the IMACS spectra. We also thank J. Scott for providing the combined FUSE spectrum of PG 1216+069. This research has made use of the NASA/IPAC Extragalactic Database (NED) which is operated by the Jet Propulsion Laboratory, California Institute of Technology, under contract with the National Aeronautics and Space Administration. H.-W.C. acknowledges partial support from NASA Long Term Space Astrophysics grant NNG06GC36G and an NSF grant AST-0607510. JSM acknowledges partial support for this work from NASA grant NNG04GC846.

REFERENCES

- Bertin, E. & Arnouts, S. 1996, *A&AS*, 117, 393
 Blanton, M. R. et al. 2003, *ApJ*, 592, 819
 Bond, N. A., Churchill, C. W., Charlton, J. C., & Vogt, S. S. 2001, *ApJ*, 557, 761
 Bournaud, F., Duc, P.-A., Amram, P., Combes, F., & Gach, J.-L. 2004, *A&A*, 425, 813
 Carswell, R. F., Lanzetta, K. M., Parnell, H. C., & Webb, J. K. 1991, *ApJ*, 371, 36
 Cen, R. & Ostriker, J. P. 2006, 650, 573
 Chen, H.-W., Lanzetta, K. M., Webb, J. K., & Barcons, X. 1998, *ApJ*, 498, 77
 ———, 2001a, *ApJ*, 559, 654
 Chen, H.-W. & Prochaska, J. X. 2000, *ApJ*, 543, L9
 Chen, H.-W., Lanzetta, K. M., & Webb, J. K. 2001b, *ApJ*, 556, 158
 Chen, H.-W., Prochaska, J. X., Weiner, B. J., Mulchaey, J. S., & Williger, G. M. 2005, *ApJ*, 629, L25
 Chen, H.-W. & Tinker, J. L. 2008, *ApJ*, 687, 745
 Churchill, C. W., Kacprzak, G. G., Steidel, C. C., & Evans, J. L. 2007, *ApJ*, 661, 714
 Coleman, G. D., Wu, C. C., & Weedman, D. W. 1980, *ApJS*, 43, 393
 Cooksey, K. L., Prochaska, J. X., Chen, H.-W., Mulchaey, J. S., & Weiner, B. J. 2008, *ApJ*, 676, 262
 Davé, R., Cen, R., Ostriker, J. P., Bryan, G. L., Hernquist, L., Katz, N., Weinberg, D. H., Norman, M. L., & O’Shea, B. 2001, *ApJ*, 552, 473
 Dobrzycki, A., Bechtold, J., Scott, J., & Morita, M. 2002, *ApJ*, 571, 654
 Dressler, A., Hare, T., Bigelow, B. C., & Osip, D. J. 2006, *Proc. SPIE*, 6269, 13
 Elmegreen, D. M., Elmegreen, B. G., Ferguson, T., & Mullan, B. 2007, *ApJ*, 663, 734
 Fukugita, M., Hogan, C. J., & Peebles, P. J. E. 1998, *Nature*, 503, 518
 Fukugita, M. 2004, in *IAU Symp. 220, Dark Matter in Galaxies*, ed. S. D. Ryder et al. (San Francisco: ASP), 227
 Grogin, N. A. & Geller, M. J. 1998, 505, 506
 Howk, J. C., Ribaud, J. S., Lehner, N., Prochaska, J. X., & Chen, H.-W. 2009, *ApJ* submitted
 Jannuzi, B. T. et al. 1998, *ApJS*, 118, 1
 Kawata, D. & Rauch, M. 2007, *ApJ*, 663, 38
 Landolt, A. U. 1992, *AJ*, 104, 340
 Landy, S. D. & Szalay, A. S. 1993, *ApJ*, 412, 64
 Lanzetta, K. M., Bowen, D. V., Tytler, D., & Webb, J. K. 1995, *ApJ*, 442, 538
 Lehner, N., Savage, B. D., Wakker, B. P., Sembach, K. R., & Tripp, T. M. 2006, *ApJS*, 164, 1
 Lehner, N., Savage, B. D., Richter, P., Sembach, K. R., Tripp, T. M., & Wakker, B. P. 2007, *ApJ*, 658, 680
 Lehner, N., Prochaska, J. X., Kobulnicky, H. A., Cooksey, K. L., Howk, J. C., Williger, G. M., & Cales, S. L. 2009, *ApJ* in press (arXiv:0812.4231)
 Li, C., Kauffmann, G., Heckman, T. M., White, S. D. M., & Jing, Y. P. 2008, *MNRAS*, 385, 1915
 Madgwick, D. S. et al. 2003, *MNRAS*, 344, 847
 Maller, A. H. & Bullock, J. S. 2004, *MNRAS*, 355, 694
 Mo, H. J. & Miralda-Escudé, J. 1996, *ApJ*, 469, 589
 Mo, H. J. & White, S. D. M. 2002, *MNRAS*, 336, 112
 Morris, S. L., Weymann, R. J., Dressler, A., McCarthy, P. J., Smith, B. A., Terrielle, R. J., Giovanelli, R., & Irwin, M. 1993, *ApJ*, 419, 524
 Mulchaey, J. S., Mushotzky, R. F., Burstein, D., & Davis, D. S. 1996, *ApJ*, 456, L5
 Mulchaey, J. S. & Chen, H.-W. 2009, *ApJ* submitted
 Oppenheimer, B. D. & Davé, R. 2009, *MNRAS* submitted (arXiv:0806.2866)
 Penton, S. V., Stocke, J. T., & Shull, J. M. 2002, *ApJ*, 565, 720
 ———, 2004, *ApJS*, 152, 29
 Persic, M. & Salucci, P. 1992, *MNRAS*, 258, 14
 Pickles, A. J. 1998, *PASP*, 110, 863
 Prochaska, J. X., Chen, H.-W., Howk, J. C., Weiner, B. J., & Mulchaey, J. S. 2004, *ApJ*, 617, 718
 Prochaska, J. X., Weiner, B. J., Chen, H.-W., & Mulchaey, J. S. 2006, *ApJ*, 642, 989
 Rauch, M., Miralda-Escudé, J., Sargent, W. L. W., Barlow, T. A., Weinberg, D. H., Hernquist, L., Katz, N., Cen, R., Ostriker, J. P. 1997, *ApJ*, 489, 7
 Rauch, M. 1998, *ARA&A*, 36, 267
 Savage, B. D., Lehner, N., Wakker, B. P., Sembach, K. R., & Tripp, T. M. 2005, *ApJ*, 626, 776
 Scott, J. E., Kriss, G. A., Brotherton, M., Green, R. F., Hutchings, J., Shull, J. M., & Zheng, W. 2004, *ApJ*, 615, 135
 Sembach, K. R., Wakker, B. P., Savage, B. D., Richter, P., Meade, M., Shull, J. M., Jenkins, E. B., Sonneborn, G., & Moos, H. W. 2003, *ApJS*, 146, 165
 Sheth, R. K., Connolly, A. J., & Skibba, R. 2005, *astro-ph/0511773*
 Simcoe, R. A., Sargent, W. L. W., & Rauch, M. 2002, *ApJ*, 578, 737
 Spinrad, H., Filippenko, A. V., Yee, H. K., Ellingson, E., Blades, J. C., Bahcall, J. N., Jannuzi, B. T., Bechtold, J., & Dobrzycki, A. 1993, *AJ*, 106, 1
 Steidel, C. C., Dickinson, M., & Persson, S. E. 1994, *ApJL*, 437, L75
 Stocke, J. T., Shull, J. M., Penton, S., Donahue, M., & Carilli, C. 1995, *ApJ*, 451, 24

- Stocke, J. T., Penton, S. V., Danforth, C. W., Shull, J. M., Tumlinson, J., & McLin, K. M. 2006, *ApJ*, 641, 217
- Thom, C. & Chen, H.-W. 2008a, *ApJ*, 683, 22
- _____. 2008b, *ApJS*, 179, 37
- Thom, C., Peek, J. E., Putman, M. E., Heiles, C., Peek, K. M. G., & Wilhelm, R. 2008, *ApJ*, 684, 364
- Tinker, J. L., Weinberg, D. H., Zheng, Z., & Zehavi, I. 2005, *ApJ*, 631, 41
- Tinker, J. L., Norberg, P., Weinberg, D. H., & Warren, M. S. 2007, *ApJ*, 659, 877
- Tinker, J. L. & Chen, H.-W. 2008, *ApJ*, 679, 1218
- Tripp, T. M., Savage, B. D., & Jenkins, E. B. 2000, *ApJ*, 534, L1
- Tripp, T. M., Sembach, K. R., Bowen, D. V., Savage, B. D., Jenkins, E. B., Lehner, N., & Richter, P. 2008, *ApJS*, 177, 39
- Verner, D.A., Tytler, D., & Barthel, P.D. 1994, *ApJ*, 430, 186
- Wang, B. 1993, *ApJ*, 415, 174
- Weymann, R. J. et al. 1998, *ApJ*, 506, 1
- Williger, G. M. et al. 2006, *ApJ*, 636, 631
- Wilman, R. J., Morris, S. L., Jannuzi, B. T., Davé, R., & Shone, A. M., 2007, *MNRAS*, 375, 735
- Yip, C. W. et al. 2004, *AJ*, 128, 585
- York, D. G. et al. 2000, *AJ*, 120, 1579
- Zehavi, I. et al. 2005, *ApJ*, 630, 1
- Zheng, Z., Coil, A. L., & Zehavi, I. 2007, *ApJ*, 667, 760